IN-02
3,385
P.57

NASA Contractor Report 4431

Flow Analysis and Design Optimization Methods for Nozzle Afterbody of a Hypersonic Vehicle

Oktay Baysal

GRANTS NAG1-811 and NAG1-1188
APRIL 1992

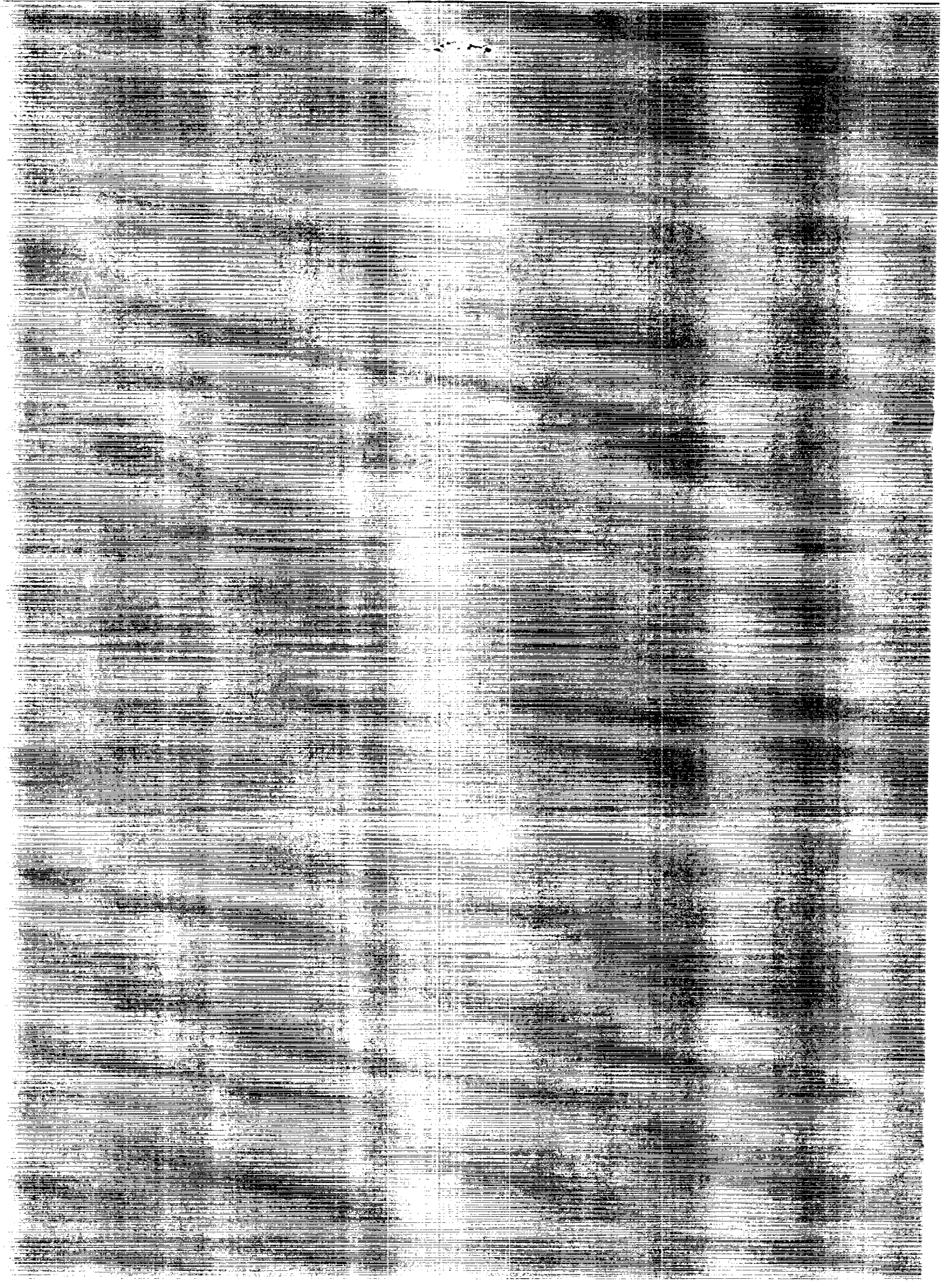

NASA Contractor Report 4431

Flow Analysis and Design Optimization Methods for Nozzle Afterbody of a Hypersonic Vehicle

Oktay Baysal
Old Dominion University
Norfolk, Virginia

Prepared for
Langley Research Center
under Grants NAG1-811 and NAG1-1188

National Aeronautics and
Space Administration

Office of Management

Scientific and Technical
Information Program

1992

TABLE OF CONTENTS

LIST OF FIGURES

Flow Analysis and Design Optimization Methods for Nozzle Afterbody of a Hypersonic Vehicle

Oktay Baysal
Old Dominion University
Norfolk, Virginia

1. INTRODUCTION

The recent resurgence of interest in hypersonic aerodynamics has come about largely in part due to the development of hypersonic vehicles, such as, the National Aerospace Plane (NASP). The design of this type of aircraft will rely heavily on the use of computational fluid dynamics, since the operating conditions prohibit the use of most of the conventional experimental facilities to obtain the required data for design analysis.

One of the major design tasks involved in the development of a hypersonic air-breathing aircraft is the integration of the engine and the airframe. This is necessary in order to reduce excessive drag and weight due to the Mach numbers at which the aircraft will be traveling. The high pressure combustion products are expanded through the combustor exit nozzle and over the airframe afterbody configuration (Fig. 1). The overall propulsive efficiency of the nozzle is determined, to a large extent, by the exhaust plume flow over this afterbody section.

The design and testing of a scramjet nozzle-afterbody section using actual engine combustion products is impractical in a conventional wind tunnel. The actual chemistry and high total enthalpy levels of the exhaust products would be quite difficult to match in a scaled test section. However, several alternatives do exist. A simulant gas can be substituted for the actual combustion products, provided that dynamic and thermodynamic similitude are enforced. Perhaps a more economical alternative would be to do the preliminary design analysis using computational fluid dynamics (CFD). Since there is currently very little experimental data for very high Mach number flows, some means of calibrating and validating these CFD codes must be achieved before they can be used with complete confidence in this design process.

In the 1970's, a study was undertaken to develop an experimental cold gas simulation technique for scramjet exhaust flows [1]. It was determined that in addition to the usual nondimensional similitude parameter requirements for inviscid flows (i.e., Mach

numbers, pressure ratios, temperature ratios, etc.), that the ratio of specific heats (γ) of the combustion products must also be matched by the simulant gases. It was also determined in this study that the surface pressures were relatively insensitive to small changes in the thermodynamic properties of the gases, but were very sensitive to flow perturbations caused by the nozzle geometry.

An extension of this work was carried out recently [2, 3]. A wind tunnel model of a single-module scramjet nozzle-afterbody configuration was constructed for testing (Fig. 2). The simulant gas mixture was fed into a high pressure plenum chamber via a mounting strut. The gas in this plenum chamber was expanded through a converging-diverging supersonic nozzle to approximately Mach 1.7 at the combustor exit plane, where it was further expanded over the nozzle-afterbody section of the model. This supersonic exhaust flow also encountered a hypersonic (Mach 6) freestream air flow, through which mixing occurred in a free shear layer containing additional expansions and shock waves. A removable tapered flow fence was used to simulate a quasi two-dimensional flow. When this fence was removed, the nozzle flow also mixed with the hypersonic freestream in the lateral direction through a spanwise expansion, causing the flow to become fully three-dimensional. Experimental data was obtained for a scaled scramjet nozzle-afterbody flowfield using both air and a Freon/Argon mixture as the simulant gas. Static pressures were measured on the afterbody surface, for both two-dimensional and three-dimensional flows, with various nozzle-afterbody geometries. Also, by using a flow rake specifically designed for this purpose, the off-surface flow was surveyed to obtain the pitot pressures. The data obtained from these experiments were used to compare with the present computational results.

The design and analysis processes for this type of nozzle-afterbody section is complex due to the fact that many additional parameters must be considered, in addition to those which must be accounted for in conventional nozzles. This particular nozzle is highly asymmetric, and consists of an internal and an external portion. The forces and moments generated by most conventional nozzles can be determined by analyzing the flow up to the nozzle exit plane only. In this particular case, the analysis must extend further downstream due to the fact that the lower aft portion of the aircraft forms the external portion of the nozzle. The flow over this afterbody region is expected to have a dramatic effect on the thrust vector and pitching moment generated by the engine module.

In the present study, a simplified configuration (Fig. 3) is assumed to model the single-module scramjet nozzle-afterbody. A rectangular duct precedes the internal nozzle. The external part of the nozzle is bounded by a ramp, a side ramp and a vertical reflection plate. The external hypersonic flow is initially over a double-corner formed by the reflection plate, the top surface of the nozzle, the exterior of the nozzle sidewall, and a side flat plate. Both of the flows expand over the 20° ramp and the side

ramp. The supersonic jet expands in the axial, the normal, and the spanwise directions after it clears the nozzle exit plane. A three-dimensional shear layer structure forms between these coflowing turbulent streams which are at a different speeds.

In this chapter, the computational methods developed for the flow analysis and the design of the aforementioned nozzle-afterbody are discussed. The three-dimensional analysis method for the air-air (simulant gas is air) flow is given in the next section. A two-dimensional, multispecies flow model is developed for the flow of Argon-Freon mixing with air, which is explained in Section 3. The results of the flow analyses are presented in Section 4. Further details of these flow analysis methods and the results obtained using them may be found in [4-9]. The last two sections are dedicated to the design optimization of the nozzle-afterbody. The methodology is described in Section 5 and some sample results are included in Section 6. More comprehensive discussion of this design optimization method may be found in [10-13].

2. ANALYSIS METHOD FOR AIR-AIR FLOW

The conservative form of the nondimensional, unsteady, compressible, Reynolds-averaged, complete Navier-Stokes equations are written below in generalized curvilinear coordinates,

$$\frac{\partial \bar{Q}}{\partial t} + \frac{\partial}{\partial \xi^m}\left(\bar{E} - \bar{E}_v\right)_m = 0; \qquad m = 1,2,3 \tag{2.1}$$

where

$$\bar{Q} = [\rho, \rho u_1, \rho u_2, \rho u_3, \rho e]^T / J \tag{2.2}$$

The symbols t, ρ, u_i, e denote the time, the density, the Cartesian velocity components and the total energy, respectively. The inviscid fluxes, viscous fluxes, and the coordinate transformation jacobian are denoted by E, E_v, and J, respectively. The state equations are written assuming air to be a perfect gas. Molecular viscosity is calculated using the Sutherland's law and the Stoke's hypothesis.

A finite volume differencing is formulated by integrating the conservation equations over a stationary control volume,

$$\frac{\partial}{\partial t}\int\int\int \bar{Q} d\Omega + \int\int \bar{E} \cdot \bar{n} dS = 0 \tag{2.3}$$

where $\bar{n}$ is the unit normal vector pointing outward from the surface S bounding the volume Ω. This implicit and second-order accurate method is described in [14, 15]. The flux-difference splitting [16] is used to construct the upwind differences for the convective and pressure terms. Spatial derivatives are written conservatively as flux balances across the cell. The Roe-averaged cell interface values of fluxes are evaluated after a state variable interpolation where the primitive variables are used.

The diffusion terms are centrally differenced. Spatial approximate factorization and Euler backward integration after linearization in time, result in the solution through 5×5 block-tridiagonal matrix inversions in each of the three directions.

The modeling of the stresses resulting from the Reynolds averaging of the governing equations is complicated by the fact that several length scales exist which control the generation, transport, and dissipation of turbulent kinetic energy. Therefore, the standard two-layer algebraic turbulence model of Baldwin and Lomax [17] is modified and used herein. It is based on the Boussinesq approximation of modeling the Reynolds stresses by an eddy viscosity, ε. That is, the Reynolds stresses and heat fluxes are assumed proportional to the laminar stress tensor with the coefficient of proportionality defined as the eddy viscosity coefficient.

Three specific modifications have been made to the standard Baldwin-Lomax model to account for: (a) vortex-boundary layer interaction and separation, (b) presence of multiple walls, and (c) turbulent memory effects in addition to the local equilibrium for the shear layer. The details of these modifications are given in [9].

The computational domain (11.1 in. by 8.1 in. by 6.6 in.) consists of the region above the cowl and to the right of the side wall where the flow is hypersonic, and another region bounded by the lower surface of the cowl and the ramp, where the supersonic internal nozzle flow expands (Fig. 3). The global grid, which consists of 808,848 cells, is block-structured with eight subdomains in order to ease the grid generation [8, 9]. The grid lines are contiguous across the block interfaces, where the solutions are matched with flux conservation. The step sizes normal to the wall vary in the range of 10^{-5} to 10^{-4} with respect to the throat height. The grid is also longitudinally clustered around the corners inside the nozzle, where the expansions occur. The step sizes for the shear layer vary from 10^{-4} to 10^{-3} with respect to the ramp length in the ζ-direction.

The upstream boundaries for the external and internal regions require specifying a viscous, double-corner flow (Fig. 4) profile and a viscous, duct (Fig. 5) profile, respectively [8, 9]. Generating such profiles requires solving the three-dimensional compressible Navier-Stokes equations. The boundary layer thickness of the final cross-plane profile of the duct flow, which is used as the upstream boundary condition for the nozzle, is approximately 0.072 in. on all four walls (Fig. 4). In addition to the boundary layer growth on the walls and in the corner regions of the external double-corner, the interaction of the two co-flowing hypersonic flows are computationally captured (Fig. 5).

No slip, impermeability, adiabatic, and zero-normal-gradient of pressure conditions are imposed on all solid surfaces. First-order extrapolation for the conserved variables are used at the downstream boundary. The outer boundary conditions are specified after

checking the sign of the normal contravariant velocity; extrapolation is used if the flow is outward and freestream values are used if the flow is inward.

The solution is obtained on two coarser level grids, and finally the finest grid, in an attempt to overcome the initial numerical transients. This approach is commonly known as mesh sequencing [14]. The residual and the normal force histories are used to determine the solution convergence. The convergence is deemed to be achieved when the residual is decreased by four orders of magnitude. An examination of the normal force coefficient, C_N, reveals an asymptotic approach to a constant value after 1500 work units. A work unit corresponds to the amount of iterations on any combination of coarse or fine grids, which requires the same amount of computer time necessary to perform one iteration on the finest grid [14]. The solution is terminated at approximately 2300 work units, in which 300 work units are performed on coarser levels. This amounts to roughly 30 hours on the CRAY-2 of NASA Langley Research Center.

3. ANALYSIS METHOD FOR MULTISPECIES FLOW

This method requires solving more equations than the method for the air flow due to the multispecies gases. Therefore, it is shown here in two-dimensions for brevity and computational time savings. Extending it to three-dimensions is rather straightforward.

The conservation form of the two-dimensional, Reynolds-averaged Navier-Stokes equations for unsteady, compressible flows of multispecies fluids is being solved. The nondimensional indicial form (i and j are dummy indices) of these equations in the Cartesian coordinates is given by

$$\frac{\partial \bar{Q}}{\partial t} + \frac{\partial E_i}{\partial X_i} = 0; \qquad i = 1, 2 \tag{3.1}$$

where

$$\bar{Q} = [\rho, \rho u_i, \rho e, \rho f_s]^T; \qquad s = 1, 2, \ldots, N-1 \tag{3.2}$$

$$E_i = [\rho u_i, \rho u_i u_j + \delta_{ij} p - \tau_{ij}, (\rho e + p) u_i - u_i \tau_{ij} + \dot{q}_i, \rho u_i f_s + DMTF_i]^T; \qquad j = 1, 2 \tag{3.3}$$

The mass fraction and pressure are denoted by f and p, respectively. N is the number of species and indices r and s indicate species. The expressions for the shear stresses and the heat flux are given as

$$\tau_{ij} = \frac{M}{Re}\left[\mu\left(\frac{\partial u_i}{\partial x_j} + \frac{\partial u_j}{\partial x_i}\right) + \lambda\left(\frac{\partial u_i}{\partial x_j}\right)\delta_{ij}\right] \tag{3.4}$$

$$\dot{q}_i = -C_p\left(\frac{\mu}{Pr} + \frac{\varepsilon}{Pr_t}\right)\frac{\partial T}{\partial x_i} + DMTE_i \tag{3.5}$$

Prandtl, Mach, and Reynolds numbers are denoted by Pr, M, and Re, respectively. First and second viscosity coefficients are shown by μ and λ. T denotes the temperature and subscript (t) denotes a turbulent quantity. C_p is the specific heat. In the above system, all the gases are assumed to be thermally perfect but calorically real gases. Hence, the enthalpy (h) of each species (s), the total energy, and the pressure can be expressed as:

$$h_s = h_s^o + \int_o^T C_{ps} dT \tag{3.6}$$

$$e = h_s f_s - \frac{p}{\rho} + \frac{1}{2}(u_i u_i) \tag{3.7}$$

$$p = \rho RT\left(\frac{f_s}{w_s}\right) \tag{3.8}$$

The enthalpy of formation, universal gas constant, and molecular weight are denoted by h^o, R, and w, respectively. The terms $DMTF_i$ and $DMTE_i$ in Eqs. (3.3) and (3.5) account for the diffusive mass transfer. The expressions for these terms depend on the utilized diffusion model. In case of using Fick's law, these terms take the form

$$DMTF_i = -\rho D \frac{\partial f_s}{\partial x_i} \tag{3.9}$$

$$DMTE_i = -\sum_{s=1}^{N} \rho D h_s \frac{\partial f_s}{\partial x_i} \tag{3.10}$$

The diffusion coefficient is denoted by D. When using a reduced form of the multicomponent diffusion equation [18] derived from the complete kinetic theory to determine the diffusion velocity components, these terms take the form

$$DMTF_i = \rho \tilde{u}_{ir} f_s \delta_{rs} \qquad r = 1, 2, \ldots, N \tag{3.11}$$

$$DMTE_i = \sum_{s=1}^{N} \rho h_s f_s \tilde{u}_{is} \tag{3.12}$$

The diffusion velocity components are denoted by $\tilde{u}$. The reduced form of the multicomponent diffusion equation is

$$\nabla X_s = \left[\sum_{r=1}^{N}\left(\frac{X_s X_r}{D}\right)\left(\tilde{V}_r - \tilde{V}_s\right)\right] + (f_s - X_s)\frac{\nabla p}{p} \tag{3.13}$$

and

$$D_{rs} = \frac{0.001858\sqrt{T^3[(w_r + w_s)/(w_r w_s)]}}{p\sigma_{rs}^2 \Omega_{rs}} \tag{3.14}$$

Eq. (3.13) is based on the assumptions that there is no thermal diffusion and that the same body force per unit mass is acting upon each species. X, σ, and Ω denote the species mole fraction, effective collision diameter, and collision integral, respectively.

Since for most turbulent mixing problems the Lewis number, which is the ratio of the Prandtl and Schmidt (Sc) numbers, is approximately unity, the expression for the effective diffusion coefficient is given by

$$\rho D = \left(D_{rs} + \frac{\varepsilon}{Sc_t} \right) \tag{3.15}$$

In Eq. (3.15), D_{rs} can be found from Eq. (3.14) when using the multicomponent diffusion model, or from the relation ($\rho D_{rs} = \mu/Sc$) when using Fick's law by specifying the Schmidt number ($Sc = 0.22$).

To calculate the required thermodynamic quantities, the specific heat for each species is defined by a fourth-order polynomial in temperature, whose coefficients are found by a curve fit to the available data. The molecular viscosity and the thermal conductivity coefficients for each species are computed from Sutherland's formula. Their values for a mixture of gases are determined from Wilke's law as follows,

$$\mu = \sum_{s=1}^{N} \left(\mu_s X_s / \sum_{\substack{r=1 \\ r \neq s}}^{N} X_r \phi_{rs} \right) \tag{3.16}$$

where

$$\phi_{rs} = \frac{\left[1 + (\mu_s/\mu_r)^{1/2} (w_r/w_s)^{1/4} \right]^2}{\sqrt{8}\ [1 + (w_s/w_r)]^{1/2}} \tag{3.17}$$

Further details of determining the binary diffusion coefficients, Sutherland constants, and the coefficients of the polynomials for the specific heat of each species are given in [4, 5].

For a two-dimensional mixing flow of N species, there are $(N-1)$ species continuity equations along with the global continuity equation, two momentum equations, and the energy equation. The mass fraction of the Nth species, f_N, can be found from the following identity

$$\sum_{s=1}^{N} f_s = 1 \tag{3.18}$$

Therefore, (N + 3) coupled partial differential equations [Eq. (3.1)] need to be solved for the vector of conserved quantities [Eq. (3.2)]. However, in an attempt to compute the global mass conservation error, the computations are repeated by solving N species continuity equations, that is, a total of (N + 4) coupled equations.

The explicit MacCormack [19] algorithm is used to solve the governing equations. The present implementation of this well-documented [20, 21] predictor-corrector scheme is based on the finite difference discretization. The type of differencing is alternated at every other time step for symmetric computations. The stress terms [Eq. (3.4)] are differenced in the direction opposite to those of the fluxes. The scheme is only conditionally stable and is second-order accurate both temporally and spatially. Fourth-order damping terms are added for shock capturing.

The diffusion velocities $\tilde{V}$ are calculated using two different models, which are the complete multicomponent diffusive interaction model, and the simple binary interaction model. In the binary model, mass diffusivities of all the species are assumed identical, and only concentration gradient effects are included [Eqs. (3.9) and (3.10)]. Whereas in the complete multicomponent model, the mass diffusivity of each species is computed using Eq. (3.14). Then, the diffusion velocity of each species is determined from Eq. (3.13), which requires solving (N) simultaneous algebraic equations for each component of the velocity. It should be noted that for N species, however, the system of N equations defined by Eq. (3.13) is not linearly independent. Therefore, one of the equations must be replaced by the following constraint

$$\sum_{s=1}^{N} \rho f_s \tilde{V} = 0 \tag{3.19}$$

The resulting system of algebraic equations is solved using a lower-upper (LU) decomposition method. When solving (N) species continuity equations, this model [Eqs. (3.11-3.14)] cannot be applied, because Eqs. (3.18) and (3.19) can no longer be satisfied in an exact manner due to the computational error.

The local mass error, LME, distribution due to the modeling of the multispecies mixing is computed from the formula below, which is evaluated at every grid point

$$LME = \rho - \sum_{s=1}^{N} \rho_s \tag{3.20}$$

The global mass conservation error is also computed by numerically integrating the mass along the computational domain boundaries.

The two-dimensional computational domain includes a region above the cowl where the flow is hypersonic. The rest of the computational domain is bounded by the lower

surface of the cowl and the ramp, where the supersonic flow through the internal nozzle expands (Fig. 6). This computational domain is selected to be (18.5 h by 14 h), where h is the throat height, and it corresponds to the longitudinal plane located at the half-span of the internal nozzle (Fig. 3). The cowl and the ramp angles are 12 deg and 20 deg, respectively. A fixed, boundary fitted grid is generated with appropriate clustering in the regions where high-flow gradients are expected. The global grid, which consists of 8,839 cells, is divided into four blocks. The grid lines are contiguous across the block interfaces, where the solutions from each side of the interface are matched. In the normal direction, the cowl separates blocks 1 and 2, and a horizontal line extending from the cowl tip to the downstream separates blocks 3 and 4. In the streamwise direction, the normal line at the cowl tip separates blocks 1 and 3, and blocks 2 and 4. This multiblock approach of domain decomposition alleviates the numerical errors that might occur if the boundaries and the interior of the cowl were included in the computational grids [4].

The governing equations are initially solved on this fixed grid until the global error is reduced by about 2 orders of magnitude. Then the grid is adapted to the current local flowfield solution using the two-dimensional spring-analogy approach of [22]. This grid adaptation procedure enhances the solution by reducing the global error by another 2 orders of magnitude.

The adaptation is done as a sequence of one-dimensional operations. For example, the operation starts in the ξ direction by redistributing the grid points according to a specified weighting function starting from the $\zeta = 0$ line to the $\zeta = \zeta_{max}$ line. Then the process is repeated in the ζ direction on the ξ lines. The weighting function, in the present study, is derived from the gradient of the composite function, [0.5 ρ + 0.3 u + 0.2 γ], a specified minimum step size, and a specified maximum step size. The ζ direction adaptations are performed separately for the region above the cowl (blocks 1 and 3) and the region below the cowl (blocks 2 and 4). The ξ direction adaptations are also performed separately, first for block 1, then for block 2, and finally for blocks 3 and 4 together. At the end, all these separate parts are blended together by the adaptations applied only to the block interfaces. This practice ensures maintaining the original shape of the cowl and the block interfaces. Further details of this flow-adaptive grid scheme, including the necessary equations, are given in [22] and its implementation is described in [5, 6].

4. RESULTS OF FLOWFIELD ANALYSES

The upstream conditions of the nozzle exhaust flow and the external flow are given in Table 4.1. All of the flows are considered to be fully turbulent. Only case 1 assumes the exhaust gases to be air. The cold gas simulating the exhaust gases is the Freon-12–argon mixture for cases 2–5. Presented in Table 4.2 are the computational models

for these cases. Only case 1 is computed both in two-dimensions and three-dimensions. The computations for the other cases are in two-dimensions. Cases 1 and 5 assume homogenous composition of the fluids everywhere and at all times. Therefore, the species continuity equations and the terms representing the multispecies mixing are not used for cases 1 and 5. Computed in cases 2–4 are the mixing of four species, namely, nitrogen, oxygen, Freon-12, and argon. The diffusive mass transport model derived from the complete kinetic theory is used in case 3, but the binary diffusion model is used in cases 2 and 4. Only case 4 does not assume that the sum of mass ratios of all the species is unity (Eq. 3.18).

The internal geometry for the supersonic nozzle features two corners — a lower corner at the beginning of the ramp and an upper corner upstream of the cowl tip. Two centered expansion fans develop around these corners. These two expansion fans smoothly converge at the upper corner and then propagate out into the jet plume flow. As the flow clears the internal nozzle-exit plane, two conditions can exist. When the jet static pressure is greater than the external freestream static pressure, the jet flow is underexpanded (Cases 1–4). When the static pressure of the jet is less than the freestream static pressure, the jet flow is overexpanded (Case 5).

Table 4.1 Flow conditions at upstream of computational domain

Case	Flow	Fluid (by volume)	Mach No.	Reynolds No. based on (h)	Total temp. (°K)	Total pressure (kPa)
1	Nozzle throat	Air: 79% N_2 21% O_2	1.7	192,000	475	166.0
2-5	Nozzle throat	50% Freon-12 50% Argon	1.7	7500	467	172.4
1-4	External flow	Air: 79% N_2 21% O_2	6.0	346,000	478	2517.0
5	External flow	50% Freon 12 50% Argon	1.7	7500	467	172.4

Table 4.2 Computational mixing models

Case	Multispecies mass transport	Specific heat ratio function of	Diffusive mass transport model	No. of partial differential equations solved
1	No	Temperature	—	4(2-D) or 5(3-D)
2	Yes	Temperature, Composition	Eqs. (3.9-3.10)	4 + 3
3	Yes	Temperature, Composition	Eqs. (3.11-3.14)	4 + 3
4	Yes	Temperature, Composition	Eqs. (3.9-3.10)	4 + 4
5	No	Temperature	—	4

4.1 Three-Dimensional Results:

The three-dimensional results obtained for Case 1 are shown in Figs. 7 through 11. The pitot pressure contours for an η–constant plane, located at 1.5 in. from the reflection plate, are shown in Fig. 7. Just upstream of the cowl tip, a 0.53 in. thick boundary layer is formed for the external flow. The supersonic-hypersonic mixing of air forms a shear layer downstream of the cowl tip. This shear layer behaves like an extension of the cowl and the flow continues to expand between the ramp and the shear layer. Two centered expansion fans develop around the corners inside the nozzle. A small plume shock, caused by the high-pressure expanding jet interacting with the low pressure external flow, forms at the cowl tip and deflects downward at about -10°. This shock can induce separation in the region of the cowl tip. The extent of this separation (when it exists) is highly dependent on the plume shock strength. The jet also expands in the streamwise direction. The flowfield along the ramp and side ramp contains expansion waves.

The same type of flow features are present in the spanwise direction and the jet laterally expands out into the freestream. A shear layer develops between the high-pressure, low-speed jet and the low-pressure, high-speed external flow. This leads to a plume shock as the hypersonic external flow is slowed down by the expanded jet plume. Shown in Fig. 8 are the Mach contours for a ζ-constant plane (approximately parallel to the ramp at 0.3 in.) of the afterbody configuration, where the nozzle, the ramp, and the side ramp are observed. The jet expands downstream of the nozzle, and the highly expanded lateral jet plume is clearly seen. A much thicker boundary layer develops at the side wall in comparison to the one seen in the normal direction. The higher-pressure jet causes the external hypersonic flow, approaching the nozzle exit plane, to experience

a plume shock. As a result of the spanwise expansion of the jet and this plume shock, a flow separation is started, and it propagates spanwise along the side ramp.

A more comprehensive view of the afterbody flowfield is shown through its crossflow Mach contours in Fig. 9. Expansion is seen in normal, spanwise, and streamwise directions. The growths of turbulent boundary layers on the reflection plate, ramp, and side ramp are evident. The exiting jet transforms from a rectangular shape at the nozzle exit plane to an enlarged elliptical plume as the flow propagates downstream. Obviously, this affects the shape of the resulting three-dimensional shear layer.

Computational off-surface pitot pressure, P_p, values are compared with the experimental results [3] in Fig. 10. Four separate rake stations (Station 1 is located at the nozzle exit plane), each containing 25 pitot tubes, are placed at midspan on the ramp. Here, (L) denotes the length of the rake measured approximately normal from the ramp surface, and (s) denotes the tangential distance along the ramp surface, measured from the 20° ramp corner. The numerical simulation of the shear layer is accomplished with some deviations seen in the high peak values of Stations 2, 3 and 4 located at s=3.5 in, 4.54 in, and 5.54 in, respectively. According to the experimental results, a compression wave forms at the cowl tip and extends to the third rake station at approximately −10°. The effect of this shock is seen both experimentally and computationally in the low peak values. Computational results follow the experimental trend for the shock with some deviation in location and strength. Station 3 reveals the largest discrepancy.

Comparisons of the computational and experimental [2] surface pressure coefficients on the ramp and side ramp are shown in Fig. 11. Pressure values are plotted at five spanwise locations. The first three stations (located on the ramp), which are downstream of the nozzle exit plane, exhibit high initial C_p values before gradually declining as the flow continues to expand down the ramp. The C_p distributions on the side ramp (η=3.50 in. and η=4.25 in.) are relatively constant and predict slightly lower C_p values than the final C_p value attained on the ramp. This is due to the greater spanwise expansion on the side ramp. All of the computed C_p values compare very well with their experimental values.

Discrepancies between the computational and the experimental results can be attributed mainly to the grid, the turbulence model, and the uncertainties associated with the wind tunnel data. Some improvement is possible by using a more refined initial grid followed by adapting the grid to the flow solution as it develops. Also, the boundary layer thickness used at the upstream of the internal nozzle flow (0.072 in.) is only assumed to be approximating the experiment, since boundary layer thicknesses were not measured during the wind tunnel tests [2, 3].

4.2 Two-Dimensional Results on Adaptive Grids

An overexpanded flow case is designed to check the solution method on adaptive grids (case 5). The fluid is a mixture of 72% Freon-12 and 28% Argon, by mass (46%-54%, by volume). This mixture is assumed to retain its composition uniformly everywhere, thence the computations are for the constant specific heat ratio of γ=1.214. The converged solution is obtained on the second flow-adapted grid shown in Fig. 6b. Shown in Fig. 12 are the Mach contours. The jet at the cowl tip plane is overexpanded, which results in a shock, with a pressure ratio of 2.7, impinging on the ramp. A separation bubble and a reflected weaker shock are observed. The interaction of the internal and external flows is through two expansions which emanate from the cowl tip region. The top expansion is a fan pointed upward with an included angle of about 55°. The lower expansion is directed inward interacting with the reflected shock towards the downstream, where the ratio of pressure to that of throat is 0.3. A small separation zone is also detected at the upper cowl tip.

In the remainder of this section, the multispecies flow computations, i.e. cases 2-4, will be discussed. Shown in Fig. 13 is a representative flow adaptive grid used for these cases. Presented in Fig. 14 are the computed and experimentally measured [2] pressure distributions on the ramp surface. All pressures are normalized with the pertinent pressure values at the upstream corner. The rate of expansion of airflow (case 1) is much higher than that of Freon-argon mixture (cases 2–4) at the corner. The difference between the expansion rates gradually decreases, but the pressure ratios of Freon-argon mixture are consistently higher than those of air. The computed pressure values from cases 2-4 are very close to each other. In comparison with the experimental data, they are initially slightly lower, then slightly higher. The computed values of surface pressures for the air expansion (case 1) are also slightly lower than the experimental values, but they match almost identically down the ramp.

In an attempt to assess the error associated with the assumption that the sum of computationally obtained species mass ratios is unity (Eq. 3.18), the mass deficits of cases 2 and 4 are computed (Fig. 15). The mass deficit is defined herein as the difference between the numerically integrated outflux and influx of mass through the boundaries of the computational domain. The solutions of cases 2 and 4 show convergence in about 4000 iterations (pseudo-time steps). The mass deficit is less than 1% for case 2, where the sum of the mass ratios is assumed to be unity. This is a commonly used assumption in similar mixing, multispecies computations, such as [20]. When this assumption is not made, and consequently four species continuity equations are solved for four species (case 4), the mass deficit is about 8%. A further analysis is performed in order to find multispecies mixing (Eq. 3.20) and the results are plotted in Fig. 16. This error, of course, is identically zero for the other cases. This mass error is occurring, as expected, within the shear layer, where the mixing takes place. It grows in the downstream direction to a maximum of 1%.

The contours of the specific heat ratio (γ) are plotted in Fig. 17. It varies throughout the flowfield as a function of temperature and local gas composition. In case 1, however, the variation of γ is only due to temperature. The values of γ change in the streamwise direction and the normal direction, with the large gradients being in the shear-layer and boundary-layer regions. Effects of the diffusive mass transport models can be observed by comparing Figs. 17a and 17b. The model derived from the complete kinetic theory (case 3), produces smoother shear layer and boundary layers. The binary model (cases 2 and 4), produces more oscillations, with quantitative results varying by about 2%. These oscillations exist despite the apparent converged solution of case 2 as indicated by an examination of Fig. 15. Therefore, the extra computational cost of the model used in case 3 may be justified if better accuracy and oscillation-free solutions are desired. It should be pointed out that the flows under consideration are turbulent, high-speed flows. The differences in the results from these two models are expected to be more pronounced for laminar, low-speed flows.

The mass fraction contours for Freon-12 and nitrogen are shown in Fig. 18. The fluid composition at the edges of the shear layer is slightly different from its upstream mixtures. There is a very large gradient of mixture composition through the shear layer. Some Freon-12 and argon mixture is entrained upstream with the reversed flow on the upper surface of the cowl. When Figs. 17 and 18 are inspected together, it is observed that the major cause for the variation of γ in the shear layer is the change in the composition of the multispecies fluid. In other regions, such as near the walls, the variation of γ is primarily due to temperature gradients.

5. AERODYNAMIC DESIGN OPTIMIZATION

In the previous sections, flow analysis methods and their results were presented. These are prerequisites to a design process, which is explained in this section. As it will become obvious, this process is relatively more expensive in terms of computations. Therefore, it will be demonstrated only in two-dimensions and using the inviscid flow equations for the air flow (Euler equations). Its extension to three-dimensional, viscous, multispecies flows is straightforward, but computations are certainly more costly.

It is desired to determine the nozzle ramp shape which yields a maximum axial thrust force coefficient, F, subject to constraints, G_j (Fig. 19). There are a number of ways to choose the design variables [12]. Two of them are presented here: surface grid and Bezier polynomials [23]. Since the surface grid for the inviscid analysis contains 47 points from the corner to the tip of the ramp, and the local slope at each grid rather than its coordinates are used as the design variables, the number of design variables (NDV) is 47 for the first choice. For the second choice, six control points are chosen for the Bezier polynomials. Hence, NDV is 6 for this option.

Mathematically, it is required to get

$$\max F\left(\bar{Q}(\bar{X}_D), \bar{X}_D\right) \tag{5.1}$$

subject to

$$G_j\left(\bar{Q}(\bar{X}_D), \bar{X}_D\right) \leq 0, \quad j = 1, NCON \tag{5.2}$$

$$\bar{X}_{D_{lower}} \leq \bar{X}_D \leq \bar{X}_{D_{upper}} \tag{5.3}$$

where $NCON$ is the number of constraints, and $\bar{Q}$ is the vector of the conserved variables of the fluid flow. $\bar{X}_{D_{lower}}$ and $\bar{X}_{D_{upper}}$ are the lower and the upper bounds of the design variables.

The component of the axial thrust force due to nozzle wall shape, F_{axial}, is obtained numerically by integrating the pressure, P, over the ramp and cowl surfaces. Then it is normalized by the force associated with the inflow, which is parallel to the cowl surface. For a constant inflow Mach number, M_{th}, the inflow force is centered at the mid-point of the line segment $\overline{kc}$ and its value is

$$F_{inflow} = P_{th}\left(1 + \gamma M_{th}^2\right)h \tag{5.4}$$

where h is the throat (th) height and γ is the ratio of the specific heats. By definition, the axial thrust force coefficient, F, is given in [11] as,

$$F = \frac{F_{axial}}{F_{inflow}} = \frac{\left(\int_k^l P_{ramp} dy\right) + \left(\int_m^n P_{cowl} dy\right)}{F_{inflow}} \tag{5.5}$$

This axial thrust force coefficient is subject to three physical constraints. The first constraint requires that the static pressure at the ramp tip, P_l, reaches a percentage of the free stream static pressure, P_∞, such that maximum expansion over the ramp is reached without any reverse flow. The second and third constraints require that the static pressure at the cowl tip, P_n, should be within specified limits of the free stream static pressure, such that expansion waves emanating from the ramp initial expansion do not induce any reverse flow on either the internal or external cowl surfaces.

In addition to the physical constraints stated above, there are geometrical constraints on the configuration (Fig. 19). In order to maintain the total length of the aircraft as a constant, the axial length of the ramp is fixed. Also, in order to maintain an acceptably smooth aerodynamic surface shape, upper and lower limits are imposed on the local surface coordinates, local slopes, and the Bezier control points relative to their neighbors.

This nonlinear, constrained optimization problem is solved using the modified feasible directions method developed by Vanderplaats (Ref. 24). Given a set of initial values for the design variables, the method first drives all the design variables into a feasible design space, i.e., the space where none of the design constraints are violated. Then the optimum design is methodically searched for within this space. This search is controlled by search directions which are based on the objective function gradient and, therefore, efficiently guides the succeeding calculations towards incrementally improved designs. Since this optimization process requires many evaluations of the objective function and constraints before an optimum design is reached, the process can be very expensive if a CFD analysis were performed for each evaluation. In the present study, however, the higher fidelity flow prediction method (approximate flow analysis), which is explained in Section 5.2, is performed during the one-dimensional searches of the optimization process. A complete CFD analysis is performed only when new gradients of the constraints and the objective function are needed, i.e. when the design changes substantially. A flowchart of this overall design process is presented in Fig. 20.

5.1 Sensitivity Coefficients

The derivatives of the objective function, F, and constraints, G_j, with respect to the design variables, $\bar{X}_D$, are defined as the sensitivity coefficients,

$$\nabla F \equiv \frac{dF}{d\bar{X}_D} = \frac{\partial F}{\partial \bar{X}_D} + \left(\frac{\partial F}{\partial \bar{Q}}\right)^T \cdot \frac{\partial \bar{Q}}{\partial \bar{X}_D} \tag{5.6}$$

$$\nabla G_j \equiv \frac{dG_j}{d\bar{X}_D} = \frac{\partial G_j}{\partial \bar{X}_D} + \left(\frac{\partial G_j}{\partial \bar{Q}}\right)^T \cdot \frac{\partial \bar{Q}}{\partial \bar{X}_D} \qquad j = 1, NCON \tag{5.7}$$

These derivatives have been determined in Ref. 10 for a case with two design variables (the inclination angles of the flat ramp and cowl surfaces to the horizontal) and three constraint functions using two approaches; namely, the finite difference approach and the quasi-analytical or sensitivity analysis approach. The sensitivity analysis can be performed by one of two methods; either the direct method or the adjoint variable method (Fig. 21). It is reported in [10] that if the number of design variables (NDV) is greater than the number of adjoint vectors (NCON+1), the adjoint variable method is more efficient than the direct method. Since, in the present study, the number of design variables, $\bar{X}_D$, (47 or 6) is greater than the number of adjoint vectors ($NCON+1 = 4$), the adjoint variable method is selected to determine the sensitivity coefficients.

The governing equations for a two-dimensional, steady, compressible, inviscid flow of an ideal gas with constant specific heat ratios written in the residual vector form are,

$$\bar{R}(\bar{Q}(\bar{X}_D), \bar{X}_D) = \frac{\partial \hat{f}}{\partial \xi} + \frac{\partial \hat{g}}{\partial \zeta} = 0 \tag{5.8}$$

where $\hat{f}$ and $\hat{g}$ are the flux Jacobians in generalized coordinates (ξ, ζ). These equations can be obtained by eliminating all the viscous and the mass diffusion terms in the Navier-Stokes equations for the multispecies flow given in Section 3. Equation (5.8) may be solved by two different methods for the analysis and the simulation of the flowfield. The first method is the approximately factored (AF) method (Eq. 2.4), which is explained in Section 2 and in [14-16]. The second method is using the Newton's method [25] to solve Eq. (5.8) directly. As it will be discussed in Section 6, this direct method is more efficient than the approximately factored method.

The sensitivity analysis approach [10] begins by differentiating Eq. (5.8) with respect to the design variables to yield the sensitivity equation,

$$\left[\frac{\partial \bar{R}}{\partial \bar{Q}}\right]\left\{\frac{\partial \bar{Q}}{\partial \bar{X}_D}\right\} = -\left[\frac{\partial \bar{R}}{\partial \bar{X}_D}\right] \equiv \mathbf{R}_v \tag{5.9}$$

This equation is solved for $\{\partial \bar{Q}/\partial \bar{X}_D\}$. It should be noted that Eq. (5.9) needs to be solved for each design variable, X_D; however, the coefficient matrix $[\partial \bar{R}/\partial \bar{Q}]$ needs to be factorized once and for all. The remaining partial derivatives in Eqs. (5.6) and (5.7) can be evaluated analytically using the equations of the objective function and the constraints. The final step is determining the values of ∇F and ∇G_j.

At this point, the adjoint variable method diverges from the direct method. First, Eq. (5.9) is substituted into Eqs. (5.6) and (5.7). Then, the vectors of adjoint variables ($\bar{\lambda}_1$, $\bar{\lambda}_{2j}$) are defined to satisfy the following equations,

$$J^T \bar{\lambda}_1 = \frac{\partial F}{\partial \bar{Q}} \tag{5.10}$$

$$J^T \bar{\lambda}_{2j} = \frac{\partial G_i}{\partial \bar{Q}} \qquad j = 1, NCON \tag{5.11}$$

where $J^T = \left[\partial \bar{R}/\partial \bar{Q}\right]^T$. The adjoint variable method requires the solution of Eqs. (5.10) and (5.11) for the adjoint variable vectors, and then, upon substitution into Eqs. (5.6) and (5.7), yields the derivatives of F and G_j. It should be noticed that Eqs. (5.10) and (5.11) are independent of any differentiation with respect to $\bar{X}_D$; hence, the vectors $\bar{\lambda}_1$ and $\bar{\lambda}_{2j}$ remain the same for all the elements of the vectors $\bar{X}_D$.

Various methods can be used to solve the rather large sets of algebraic equations resulting from Eqs. (5.9) or (5.10–5.11). Details and comparisons of these methods (banded method, sparse method, iterative method, etc.) are given in [10-13].

5.2 Flow Prediction Method

An approximate flow analysis method has been introduced in [10-13] to predict a flowfield solution of a perturbed shape $(\bar{X}_D^* + \Delta\bar{X}_D)$ using the flowfield solution of an initially unperturbed shape $(\bar{X}_D^*)$. This method is based on a Taylor series expansion of the vector of conserved variables $\bar{Q}(\bar{X}_D^* + \Delta\bar{X}_D)$ about $\bar{Q}(\bar{X}_D^*)$ and requires the substitution of Eq. (5.9) into the Taylor expansion:

$$\left[\frac{\partial\bar{R}(\bar{Q}(\bar{X}_D^*),\bar{X}_D^*)}{\partial\bar{Q}}\right]\Delta\bar{Q} = -\left[\frac{\partial\bar{R}(\bar{Q}(\bar{X}_D^*),\bar{X}_D^*)}{\partial\bar{X}_D}\right]\Delta\bar{X}_D \tag{5.12}$$

where

$$\Delta\bar{Q} = \bar{Q}(\bar{X}_D^* + \Delta\bar{X}_D) - \bar{Q}(\bar{X}_D^*) \tag{5.13}$$

Equation (5.13) explicitly gives the changes in $\bar{Q}$ due to the changes in $\Delta\bar{X}_D$. From here on, the term *prediction* is used when the flowfield is predicted using Eq. (5.13), and the term *analysis* is used when the complete governing equations (Eq. 5.8) are solved with the CFD algorithms described in Sections 2 and 3.

The next logical step in the prediction method is to extend the idea of prediction based on analysis to that of prediction based on prediction. Performing a parallel operation to that of Eq. (5.12), we obtain a second level flowfield prediction analogous to Eq. (5.13) by

$$\bar{Q}\left(\bar{X}_D^* + \Delta\bar{X}_D^{(1)} + \Delta\bar{X}_D^{(2)}\right) \simeq \bar{Q}\left(\bar{X}_D^* + \bar{X}_D^{(1)}\right) + \Delta\bar{Q}^{(2)} \tag{5.14}$$

where $\bar{Q}\left(\bar{X}_D^* + \Delta\bar{X}_D^{*(1)}\right)$ is obtained by Eq. (5.13). It should be noted that $\partial\bar{Q}/\partial\bar{X}_D$ in Eq. (5.14) is based on the *predicted* flowfield $\bar{Q}\left(\bar{X}_D^* + \Delta\bar{X}_D^{(1)}\right)$. This procedure allows flowfield solutions to be progressively "built up" from previous predictions; all of which have the common genesis of a single initial CFD analysis solution. Thus, a flowfield solution for a complex final shape may be obtained through incrementally additive design variable perturbations. Otherwise, a grossly erroneous prediction is produced if an equivalent single large perturbation is attempted.

Due to the truncation error of the first-order Taylor series, the flow prediction is currently less accurate than the flow analysis. However, solving flowfield prediction Eq. (5.12) costs only a small fraction of solving Eq. (5.8), since $(\partial\bar{R}/\partial\bar{Q})$ and $(\partial\bar{R}/\partial\bar{X}_D)$ are already assembled in solving the sensitivity equation (Eq. (5.9)). Therefore, for relatively small values of $\Delta\bar{X}_D$, significant time savings are realized at the expense of some accuracy.

5.3 Sensitivity of the Optimum Design

After the optimum design is obtained, it is desirable to determine the sensitivity of the optimum design with respect to the problem parameters. Such information is useful to perform trade-off analyses. For example, it may be wished to estimate what effect a specified increase in the free stream Mach number has on the optimum thrust. Mathematically, this requires the derivatives of the optimum values of the objective function and the corresponding design variables with respect to the problem parameters.

The first-order sensitivity derivative method developed in [26] is adapted for the present study. Presented in Fig. 22 is the flowchart of this process. The vector $\bar{P}$ contains the problem parameters, which are held fixed during the optimization. Using the superscript "*op*" to denote the optimum quantities, the dependence of F^{op} and $\bar{G}$ on $\bar{X}_D$ and $\bar{P}$ can be written as

$$F^{op} = F^{op}\big(\bar{Q}(\bar{X}_D^{op}(\bar{P}), \bar{P}), \bar{X}_D^{op}(\bar{P}), \bar{P}\big) \tag{5.15}$$

$$\bar{G}_a = \bar{G}_a\big(\bar{Q}(\bar{X}_D^{op}(\bar{P}), \bar{P}), \bar{X}_D^{op}(\bar{P}), \bar{P}\big) = 0 \tag{5.16}$$

where $\bar{G}_a$ is a vector containing only the active constraints at the constrained maximum. A constraint becomes an active one when its value is zero. The total optimum sensitivity derivative of the objective function with respect to a problem parameter P is obtained using the chain rule of differentiation. Any perturbation of the parameter P about its value at the initial optimum must be such that the originally active constraints remain active. For this constrained optimization problem, the first-order optimality conditions at a local optimum (commonly known as Kuhn-Tucker conditions [27]) are used. Combining the equations for the gradient of the objective function and the active constraints, and using the Kuhn-Tucker conditions result in,

$$\frac{dF^{op}}{dP} = \frac{\partial F^{op}}{\partial P} + \bar{\psi}^T \frac{\partial \bar{G}_a}{\partial P} + \left[\left(\frac{\partial F^{op}}{\partial \bar{Q}} \right)^T + \bar{\psi}^T \left(\frac{\partial \bar{G}_a}{\partial \bar{Q}} \right)^T \right] \frac{\partial \bar{Q}}{\partial P} \tag{5.17}$$

where $\bar{\psi}$ is a vector containing the Lagrangian multipliers. The derivatives of the conserved variables vector, $\bar{Q}$, with respect to the problem parameters are obtained from the following relation,

$$\bar{R}(\bar{Q}(\bar{X}_D(\bar{P}), \bar{P}), \bar{X}_D(\bar{P}), \bar{P}) = 0 \tag{5.18}$$

Differentiation of Eq. (5.18) with respect to the problem parameters and using Eq. (5.9) results in,

$$\left[\frac{\partial \bar{R}}{\partial \bar{Q}} \right] \frac{\partial \bar{Q}}{\partial \bar{P}} = - \left[\frac{\partial \bar{R}}{\partial \bar{P}} \right] \equiv \bar{R}_v \tag{5.19}$$

Solving Eq. (5.19), similar to Eq. (5.9), for $\left(\partial\bar{Q}/\partial\bar{P}\right)$ and using it with Eq. (5.17) yields the sensitivities of the objective function to the problem parameters.

Alternatively, the adjoint variable method can be used when the substitution of Eq. (5.19) into Eq. (5.17) is performed. Then, an adjoint vector $\bar{\lambda}$, that satisfies the following equation, is defined

$$J^T\bar{\lambda} = \left[\frac{\partial F^{op}}{\partial\bar{Q}} + \left(\frac{\partial\bar{G}_a}{\partial\bar{Q}}\cdot\bar{\psi}\right)\right] \tag{5.20}$$

where $J = \left[\partial\bar{R}/\partial\bar{Q}\right]$. Substitution of Eq. (5.20) into Eqs. (5.17) and (5.19) gives,

$$\frac{dF^{op}}{dP} = \frac{\partial F^{op}}{\partial P} + \bar{\psi}^T\frac{\partial\bar{G}_a}{\partial P} + \bar{\lambda}^T\bar{R}_v \tag{5.21}$$

The adjoint system of Eq. (5.20) is independent of any differentiation with respect to the problem parameters. Also, both terms on the right hand side are available from the calculations of Eqs. (5.6) and (5.7). The partial derivatives, $\partial F^{op}/\partial\bar{P}, \partial\bar{G}_a/\partial\bar{P}$ and $\partial\bar{R}/\partial\bar{P}$ can be evaluated analytically. Therefore, the sensitivity derivatives (Eq. (5.21)) are obtained after solving Eq. (5.20), evaluating the Lagrangian multipliers, and finally performing the pertinent substitutions.

Since the number of problem parameters, $\bar{P}$, (equal to seven for the present example) is greater than the number of the adjoint vectors, $\bar{\lambda}$, (equal to one for the present example), the adjoint variable method is more economical [10] for the present example.

6. RESULTS OF DESIGN OPTIMIZATION

Prior to discussing the actual optimization results, a series of cases (Cases 6–10) will be presented to demonstrate the flow prediction method in Section 6.1. Subsequently, the optimized nozzle-afterbody shape (Cases 6, 11, and 12) will be introduced in Section 6.2.

6.1 Demonstration of Flow Prediction Method

Initially, the governing equations of the flow are solved to obtain the analysis for a flat ramp surface at α=10° (Case 6). Then the ramp is deflected in such a way that a shock can be generated; a compression corner is formed at 38% length from the ramp corner by turning the surface at an angle, θ, from the ramp surface (Fig. 23). CFD analyses are performed for three values of θ: 2.5°, 5.0°, and 10° (Case 7). Finally, the flowfields for the above θ values are predicted (Case 8) using the analysis for the flat ramp surface, that is, θ=0°. In other words, the =0° configuration (Case 6) is denoted by $\left(\bar{X}^*_D\right)$ in Eqs. 5.12–5.14, and any one of the $\theta \neq 0°$ configurations (Case 8) is denoted by $\left(\bar{X}^*_D + \triangle\bar{X}_D\right)$. The flow of Case 6 over the ramp is free of shocks. However, flows

containing compression shocks, due to ramp wall perturbation ($\theta \neq 0°$), are *predicted* based on the shock-free flow.

Table 6.1 Distinguishing Features of Flow Prediction Cases

Case	Deflection Angle, θ	Flowfield Solution Method
6	0°	Analysis
7	2.5°, 5°, 10°	Analysis
8	2.5°, 5°, 10°	Prediction based on analysis of θ=0°
9	5°	Prediction based on analysis of θ=2.5°
10	5°	Prediction based on prediction of θ=2.5°

The pressure coefficient distributions along the ramp for the Cases 6, 7, and 8 are shown in Fig. 24. The analysis (Case 7) and the predicted (Case 8) results are indistinguishable up to the compression corner. The compression corner shocks are also predicted very well. As expected, discrepancies begin to appear for the larger θ values, i.e. larger design variable changes. Notice that a discontinuous physical phenomenon (shock) is predicted based on a flow which does not have that phenomenon (shock-free). The maximum deviation is only 2% for θ=2.5°, but it increases to 22% for θ=10°. These deviations can be attributed to the nonlinear nature of the shock. This is a typical trend when a nonlinear problem is solved using a method which includes some kind of local linearization. Therefore, it can be positively concluded that the prediction method, due to truncation error, exhibits increasing inaccuracies as the deflection size, $\Delta\bar{X}_D$, increases and eventually produces unacceptable solutions when the deflection becomes too large.

An issue, which appeals to the curiosity is the success of the present prediction method for the off-surface flow, particularly, when an existing change in a configuration is enlarged; for example, predicting the flow for θ=5° when the flow of θ=2.5° is given. Shown in Fig. 25 are three sets of density contours in comparison: the flow analysis of θ=2.5°, the flow predictions of θ=5.0° based on first the flow analysis of θ=2.5° (Case 9) and then the flow predictions of θ=2.5° (Case 10). Two points are noteworthy here. First, Case 9 aims at predicting the flow due to an enlarged change (θ from 2.5° to 5.0°), but not predicting a new physical phenomenon; that is, the prediction method is given a shock with which it begins. The comparison of this case with the analysis is satisfactory, despite the fact that the shock is rather strong. Secondly, this figure

illustrates the feasibility and quality of the second level prediction of Eq. 5.14. For example, the prediction of θ=5° flowfield (Case 10) is based on the Case 8 prediction for θ=2.5°, which is based on Case 6 analysis. Since the truncation error occurs twice and progressively during this process, although associated with smaller perturbations, the agreement of Case 10 is slightly less successful than that of Case 9. Therefore, it may be concluded that higher level predictions may be further used for coarse but efficient estimates of highly perturbed shapes.

6.2 Shape Optimization of Nozzle-Afterbody

Three different and arbitrary shapes are chosen as the initial design shapes for the ramp; namely, a flat ramp surface at α=10° (Case 6), a concave surface with its axis (the straight line connecting the corner point and the ramp endpoint) at α=25.7° (Case 11), and a convex surface with its axis at α=29.5° (Case 12). The slope of initial ramp expansion is 35.0° for the concave shape and 23.5° for the convex shape. The reason for starting the optimization from three different initial shapes is to determine how close the resulting optimized ramp shapes are to each other. Ideally, they should be identical irrespective of their initial shape, so that, the designer using this method in the production mode can start with any shape that is convenient. Shown in Fig. 26 is the comparison of the optimum shapes of Cases 6, 11, and 12 along with their initial shapes. The optimum shapes are almost identical for 70% of the surface and show a small difference towards the tip. When the axis angles, α, of the optimum shapes are compared, it can be seen that the difference between Cases 11 and 12 is indistinguishable (less than 0.3%) and that of Case 6 differs from them by only 3%.

The effect of the shape optimization on the interior flowfield is just as pronounced as it is on the surface properties. The Mach number contours of both initial and optimum configurations of Case 6 are presented in Fig. 27. The expansion patterns are significantly different. The rate of expansion is much higher inside the nozzle for the optimum shape, which results in a higher Mach number and less underexpanded jet at the nozzle exit plane. The consequence of this is evidenced in the shear layer, which is thinner and has a smaller angle with the horizontal for the optimum shape. Also, the expansion along the external part of the nozzle ramp is no longer predominantly in the streamwise direction, but a significant portion is in the normal direction. This indicates that cancellation of the cowl corner centered-expansion waves occurs at the optimized ramp surface, which is a characteristic feature of bell-type nozzles.

Plotted in Fig. 28 are the histories of the objective functions, F, during the optimization iterations (or commonly known as levels). The initial F value of Case 11 is the highest, and all three shapes converge to an optimum F value within 14 optimization iterations. Cases 6 and 12 have identical optimum F values to the fourth significant digit, and that of Case 11 differs from them by less than 0.5%.

The computational time for each one of the shape optimization cases is about 3.5 hours on the CRAY-YMP of Numerical Aerodynamic Simulation (NAS) of NASA. For example, Case 6 requires 180 evaluations of the objective function over the course of 14 optimization iterations. At the end of each iteration, there is a CFD analysis accompanied with the objective function evaluation for the new improved shape. This means that CFD analysis is performed 14 times, whereas, the flow prediction calculation is performed 166 times. Comparing the computational times of an analysis ($\sim$ 175 seconds) and a prediction ($\sim$ 18 seconds), it can easily be realized that the aerodynamic optimization procedure is more efficient by employing the present prediction method.

To demonstrate the relative efficiencies of the present design optimization methods, Case 11 is solved using five different procedures and their results are given in Table 6.2. In Procedure 1, the sensitivity coefficients, ∇F and ∇G, are computed by the traditional finite-difference method. In contrast, they are computed by the sensitivity analysis (SA) approach in the rest of the procedures, i.e. Procedures 2-5. The design variables in Procedures 1–3 are the local slopes at each surface grid point (47 of them), but they are the Bezier control points (6 of them) in Procedures 4 and 5. The third important difference between the procedures is the method to solve the flow equations; all but the last procedure employ the traditional approximate factorization (AF) method and the last procedure solves these equations directly using the Newton's method. Finally, Procedures 3, 4, and 5 employ the flow prediction method, but Procedures 1 and 2 use the complete CFD analyses only.

The most efficient method is Procedure 5 and it requires 2.2 hours of computing on the CRAY-2 computer of NASA Langley Research Center. The most time is required by Procedure 1, which uses all the traditional methods. The memory requirement is of the same order of magnitude for all procedures. Part of the reasons for such disparity in computational efficiencies may easily be understood by inspecting the last two columns of Table 6.2. It is noteworthy to point out that Procedure 2 requires less CFD analyses than Procedure 1. This is due to the values of the sensitivity coefficients, which are obtained much more accurately when the sensitivity analysis approach is used. Consequently, the optimizer provides a converged solution much quicker. Further details of such efficiency considerations are given in [10-13].

Table 6.2 Normalized Computational Times Required by Different Aerodynamic Optimization Procedures

Optimization Procedure	Normalized Execution Time	Required Memorey [MW][a]	No. of CFD Analyses	No. of Approx. Flow Analyses
1) AF+slopes+FD	49.2	6.1	595	0
2) AF+slopes+SA	19.7	6.1	236	0
3) AF+slopes+SA	3.75	6.1	6	230
4) AF+Bezier+SA	2.04	5.4	15	172
5) Newton's+Bezier+SA	1.00[b]	5.4	15	172

AF: Approximate Factorization
FD: Finite Difference for sensitivity
SA: Sensitivity Analysis for sensitivity coefficients
[a] grid size (41x53)
[b] cpu time = 2.2 hrs on Cray2

7. REFERENCES

1. Oman, R. A., Foreman, K. M., Leng, J., and Hopkins, H. B. Simulation of Scramjet Exhaust. NASA-CR-2494, 1975.
2. Cubbage, J. M. and Monta, W. J. Parametric Experimental Investigation of a Scramjet Nozzle at Mach 6 With Freon and Argon or Air Used for Exhaust Simulation. NASA-TP-3048, February 1991.
3. Monta, W. J. Pitot Survey of Exhaust Flow Field of a 2-D Scramjet Nozzle With Air or Freon and Argon Used for Exhaust Simulation at Mach 6. NASA-TM-4361, 1992.
4. Baysal, O., Engelund, W. C., and Tatum, K. E. Navier-Stokes Calculations of Scramjet-Afterbody Flowfields. *Advances and Applications in Computational Fluid Dynamics.* (Ed. Baysal, O.), FED-Vol. 66, pp. 49-60, ASME, New York,Nov. 1988.
5. Baysal, O., Engelund, W. C., Eleshaky, M. E., and Pittman, J. L. Adaptive Computations of Multispecies Mixing Between Scramjet Nozzle Flows and Hypersonic Freestream. AIAA Paper 89-0009, Jan. 1989.
6. Baysal, O., Eleshaky, M. E., and Engelund, W. C. Computations of Multispecies Mixing Between a Scramjet Nozzle Flow and Hypersonic Freestream. (AIAA) *Journal of Propulsion and Power*, Vol. 8, No. 1, Jan-Feb. 1992.

7. Baysal, O., Eleshaky, M. E., and Engelund, W. C. 2–D and 3-D Mixing Flow Analyses of a Scramjet-Afterbody Configuration. Paper No. 14, *Proceedings of International Conference on Hypersonic Aerodynamics*, The Royal Aeronautical Society, Sep. 1989.

8. Baysal, O. and Hoffman, W. B. Computation of Supersonic-Hypersonic Flow Through a Single-Module Scramjet Nozzle. *Proceedings of IMACS 1st International Conference on Computational Physics*, pp. 52-59. University of Colorado, Boulder, Co., June 1990.

9. Baysal, O. and Hoffman, W. B. Simulation of 3–D Shear Flow Around a Nozzle-Afterbody at High Speeds. *Advances in Numerical Simulation of Turbulent Flows*, (Ed. I. Celik, et al.), FED-Vol. 117, pp. 75-82, Joint Meeting of ASME/JSME, June 1991. Also, (ASME) *Journal of Fluids Engineering*, Vol. 114, No. 1, March 1992.

10. Baysal, O. and Eleshaky, M. E. Aerodynamic Sensitivity Analysis Methods For the Compressible Euler Equations. *Recent Advances and Applications in CFD*, (Ed. Baysal, O.), FED Vol. 103, pp. 191–202, ASME-Winter Annual Meeting, Nov. 1990. Also, (ASME) *Journal of Fluids Engineering*, Vol. 113, No. 4, Dec. 1991.

11. Baysal, O. and Eleshaky, M. E. Aerodynamic Design Optimization Using Sensitivity Analysis and Computational Fluid Dynamics. AIAA-91-0471, Jan. 1991. Also, *AIAA Journal*, Vol. 30, No. 2, Feb. 1992.

12. Baysal, O., Eleshaky, M. E., and Burgreen, G. W. Aerodynamic Shape Optimization Using Sensitivity Analysis on Third-Order Euler Equations. AIAA Paper No. 91–1577 CP, *Proceedings of 10th Computational Fluid Dynamic Conference*, pp. 573-583, June 1991.

13. Eleshaky, M. E. and Baysal, O. Airfoil Shape Optimization Using Sensitivity Analysis on Viscous Flow Equations. *Multidisciplinary Applications of CFD* (Ed. Baysal, O.), ASME-FED, Vol. 119, pp. 26–36, Winter Annual Meeting, Dec. 1991.

14. Baysal, O., Fouladi, K., and Lessard, V. R. Multigrid and Upwind Viscous Flow Solver on 3-D Overlapped/Embedded Grids. *AIAA Journal*, Vol. 29, No. 6, pp. 903–910, June 1991

15. Baysal, O., Fouladi, K., Leung, R. W., and Sheftic, J. S. Interference Flows Past Cylinder-Fin-Sting-Cavity Assemblies. AIAA Paper No. 90-3095CP, *Proceedings of 8th Applied Aerodynamics Conference*, pp. 884–892. Also, *Journal of Aircraft*, Vol. 29, No. 1, Jan. 1992.

16. Anderson, W. K., Thomas, J. L., and Van Leer B. Comparison of Finite Volume Flux Vector Splittings for the Euler Equations. *AIAA Journal*, Vol. 24, No. 9, pp. 1453–1460, Jan. 1986.

17. Baldwin, B. and Lomax, H. Thin Layer Approximation and Algebraic Model for Separated Flows. AIAA Paper 78–257, Jan. 1978.

18. Williams, F. A. *Combustion Theory*, 2nd ed., pp. 628–649, Benjamin-Cummings Publishing, Menlo Park, CA, 1985.

19. MacCormack, R. W. The Effect of Viscosity in Hypervelocity Impact Cratering. AIAA Paper 69–354, April 1969.

20. Drummond, J. P., Rogers, R. C., and Hussaini, M. Y. A Detailed Numerical Model of a Supersonic Reacting Mixing Layer. AIAA Paper 86–1424, June 1986.

21. Baysal, O. Supercomputing of Supersonic Flows Using Upwind Relaxation and MacCormack Schemes. (*ASME*) *Journal of Fluids Engineering*, Vol. 110, No. 1, pp. 62–68, March 1988.

22. Nakahashi, K. and Deiwert, G. S. Adaptive Grid Method with Application to Airfoil Flow. *AIAA Journal*, Vol. 25, No. 4, pp. 513–520, April 1987.

23. Faux, I. D. and Pratt, M. G. Computational Geometry for Design and Manufacture. Ellis Horwood Ltd. Publishers, West Sussex, England, 1979.

24. Vanderplaats, G. N., An Efficient Feasible Direction Algorithm for Design Synthesis *AIAA Journal*, Vol. 22, No. 10, pp. 1633–1640, October 1984.

25. Venkatakrishnan, V. Newton Solution of Inviscid and Viscous Problems. *AIAA Journal*, Vol. 27, No. 7, pp. 885–891, July 1989.

26. Sobieski, J. S. and Barthelemy, J. M. Optimum Sensitivity Derivatives of Objective Functions in Nonlinear Programming. *AIAA Journal*, Vol. 21, No. 6, pp. 913–915, June 1983.

27. Reklaitis, G. V., Ravindran, A., and Ragsdell, K. M. *Engineering Optimization Methods and Applications*. 1st ed., pp. 191-203, John Wiley and Sons, New York, 1983.

8. ACKNOWLEDGEMENT

This chapter was extracted from References [4-12], which were originally written by the author and his valuable graduate students (G. W. Burgreen, M. E. Eleshaky, W. C. Engelund, W. B. Hoffman). It will also appear as a chapter in a book titled, *Computational Methods in Hypersonic Aerodynamics*, to be published by Computational Mechanics Publications, Southampton, UK.

9- FIGURES

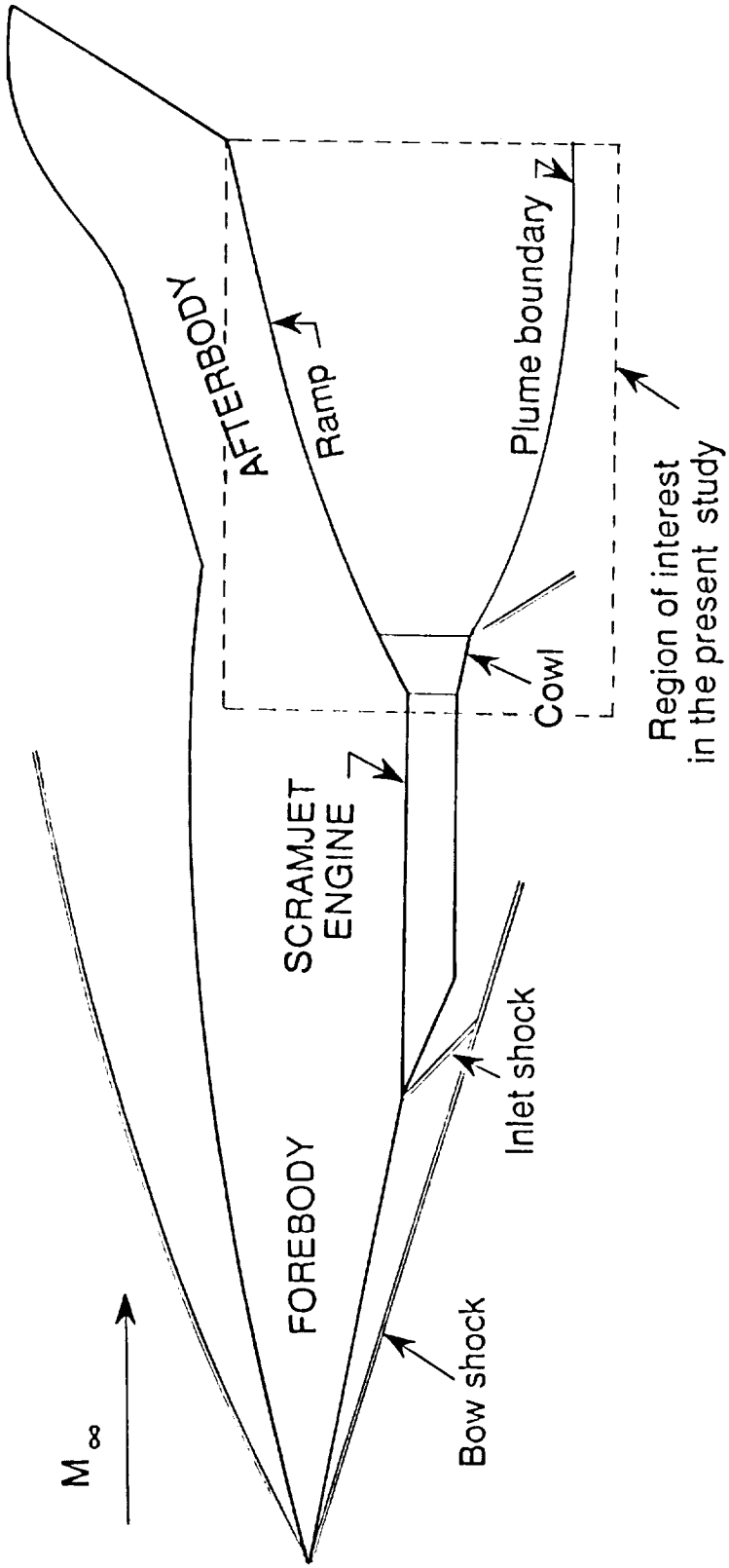

Figure 1 A schematic of the flowfield around a generic hypersonic vehicle.

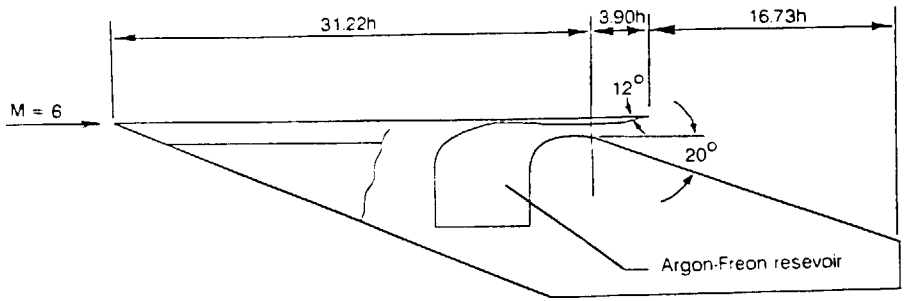

h=0.6 in.

(a)

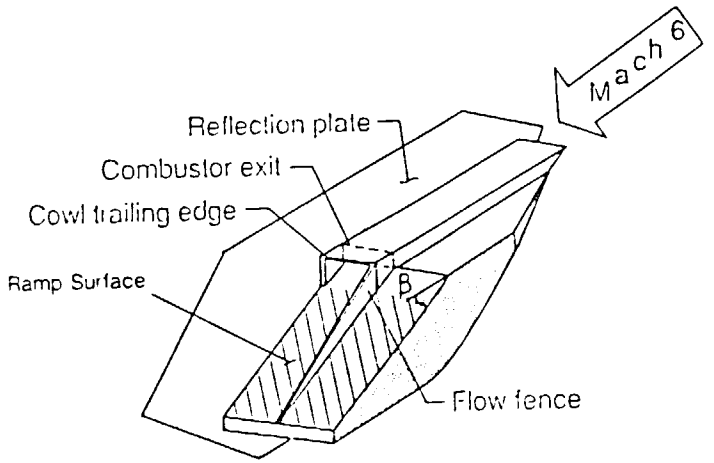

●Flow fence for quasi 2-D flow

(b)

Figure 2 A wind tunnel model of a single-module scramjet nozzle and afterbody: (a) sectional view, (b) isometric view.

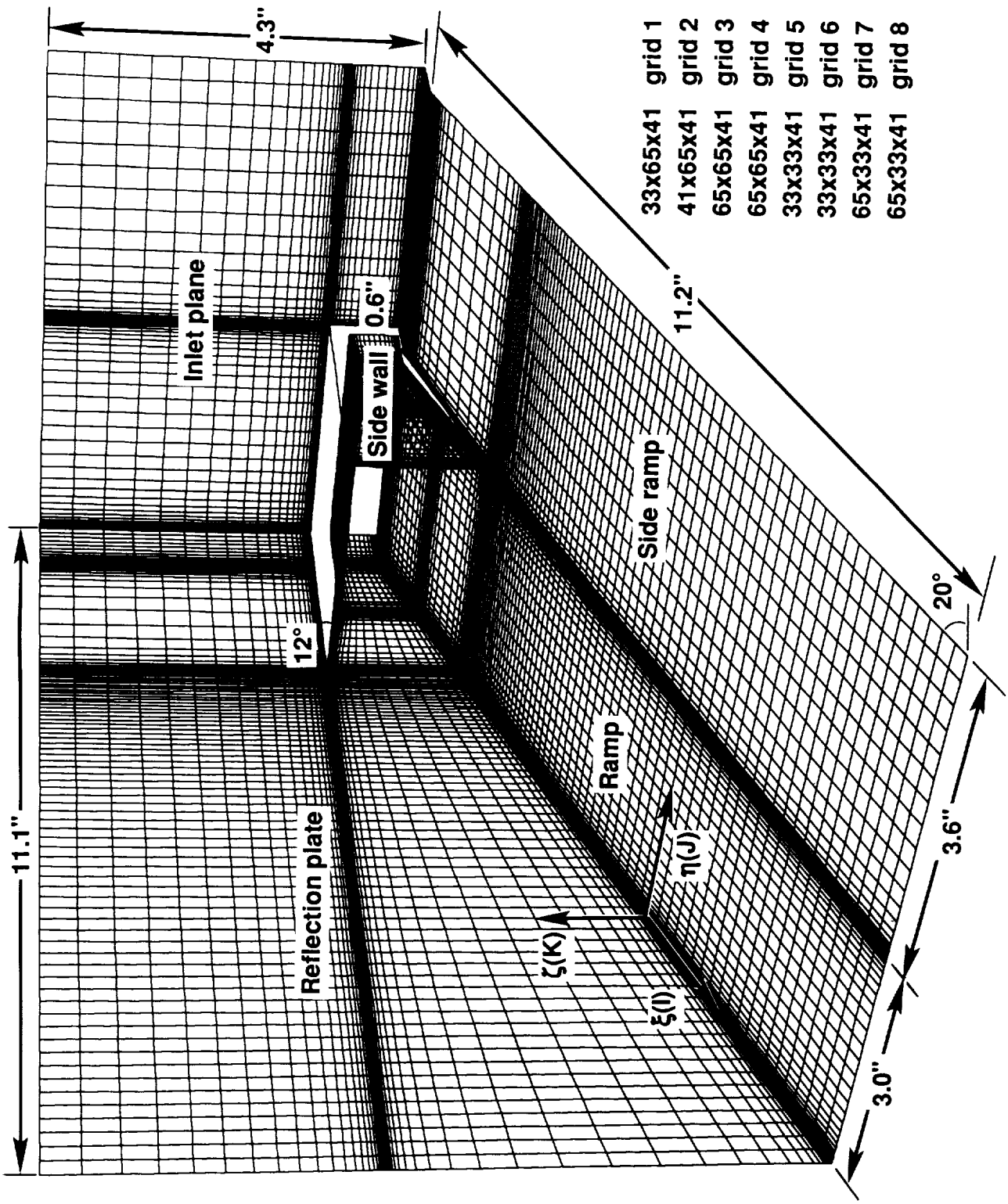

Figure 3 Three-dimensional grid for the computational model of the nozzle-afterbody. The grid is made of eight blocks and 808,848 cells.

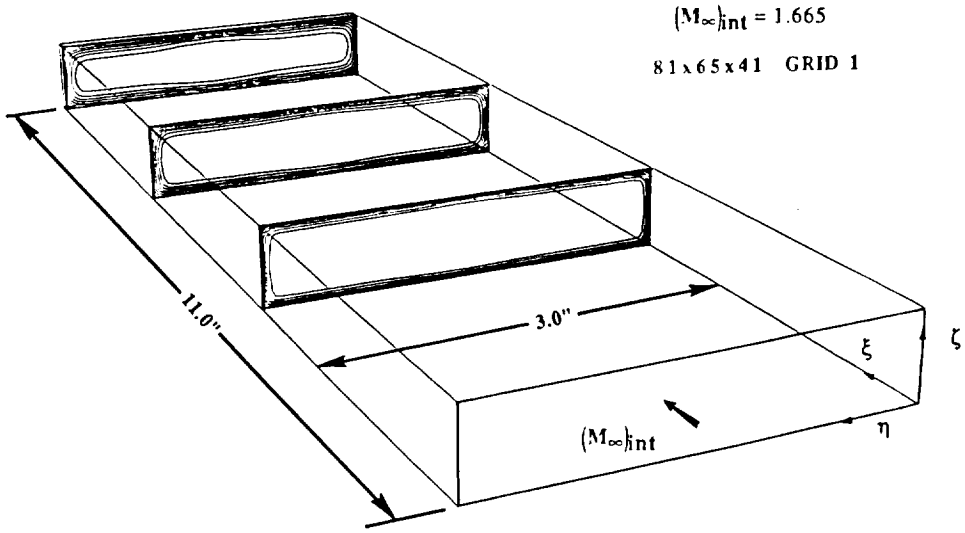

Figure 4 Mach number contours of the flow inside the rectangular duct preceding the internal nozzle (Case 1).

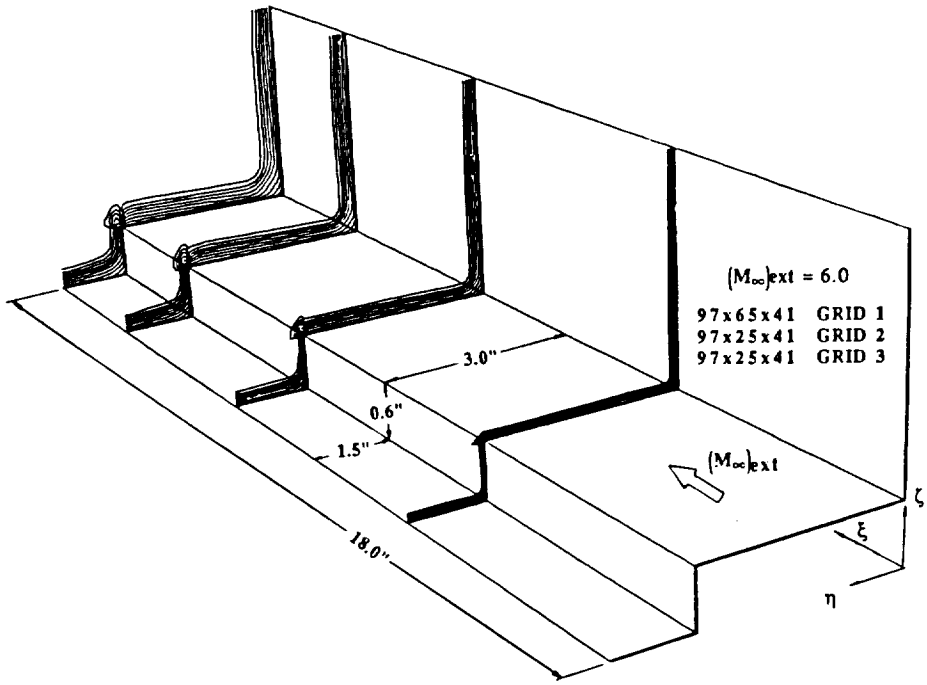

Figure 5 Mach number contours of the external flow past the double corner preceding the cowl and the external nozzle (Case 1).

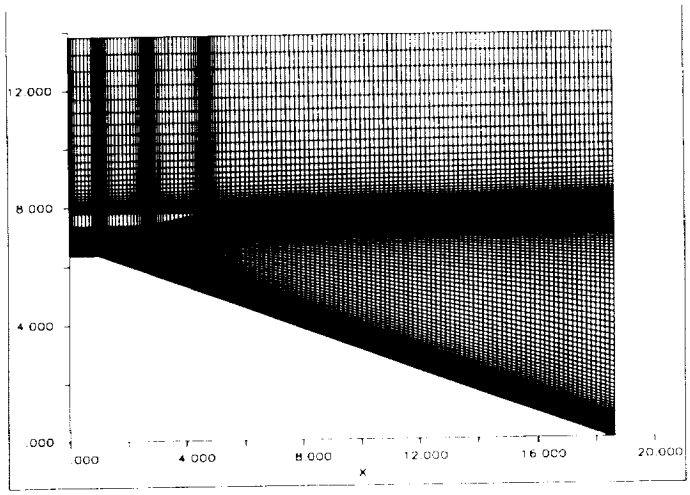

(a)

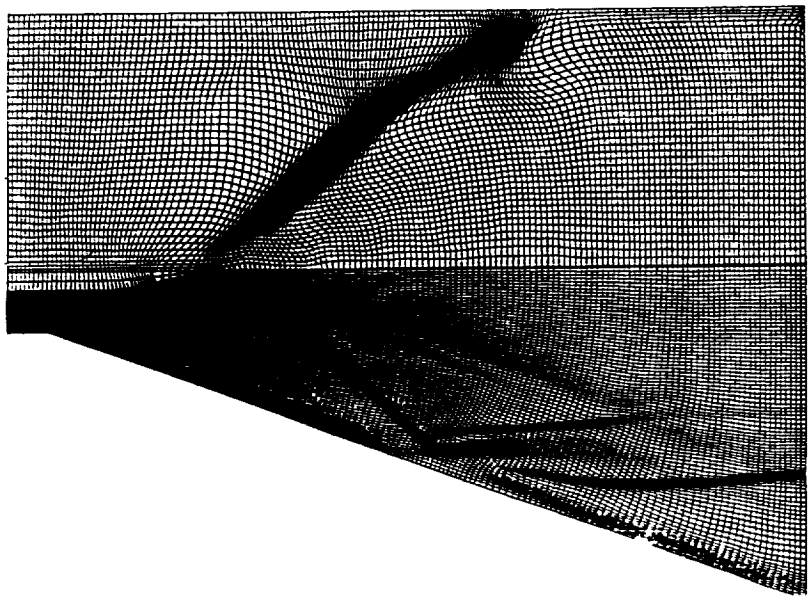

(b)

Figure 6 Grids for two-dimensional computations with 20,305 cells: (a) fixed grid, (b) flow adapted grid for Case 5.

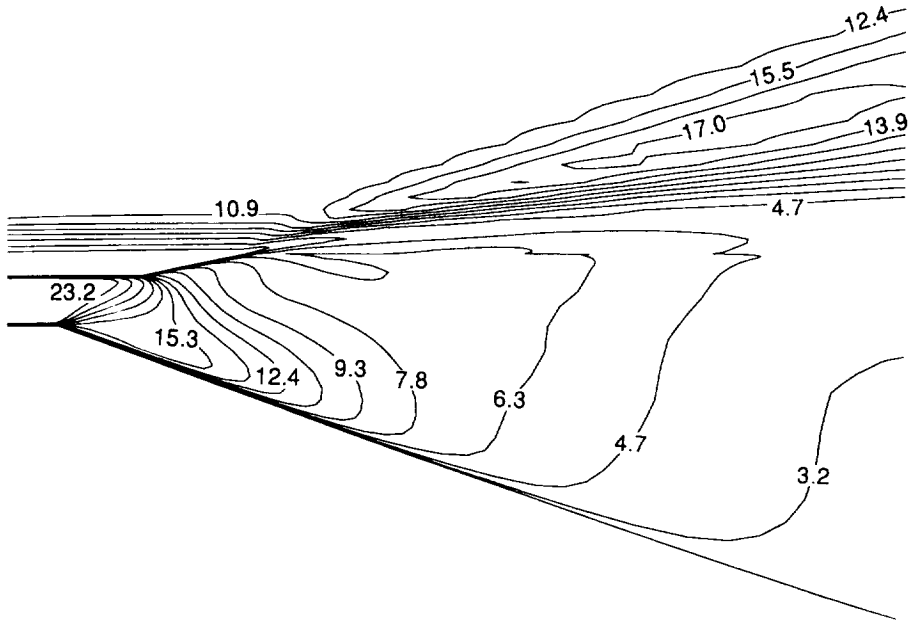

Figure 7 Pitot pressure contours in the internal nozzle and ramp region for an η-constant plane (Case 1).

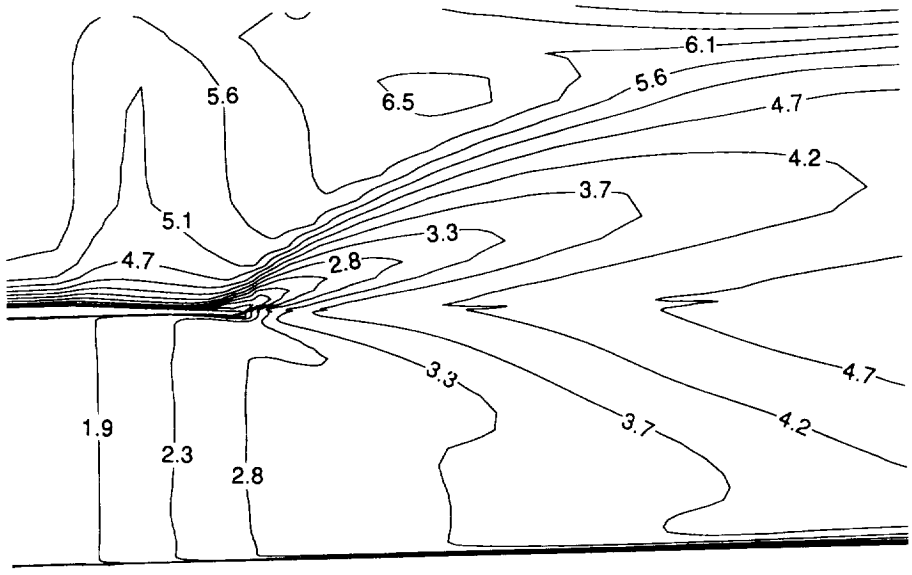

Figure 8 Mach contours for an ζ-constant plane of the nozzle-afterbody (Case 1).

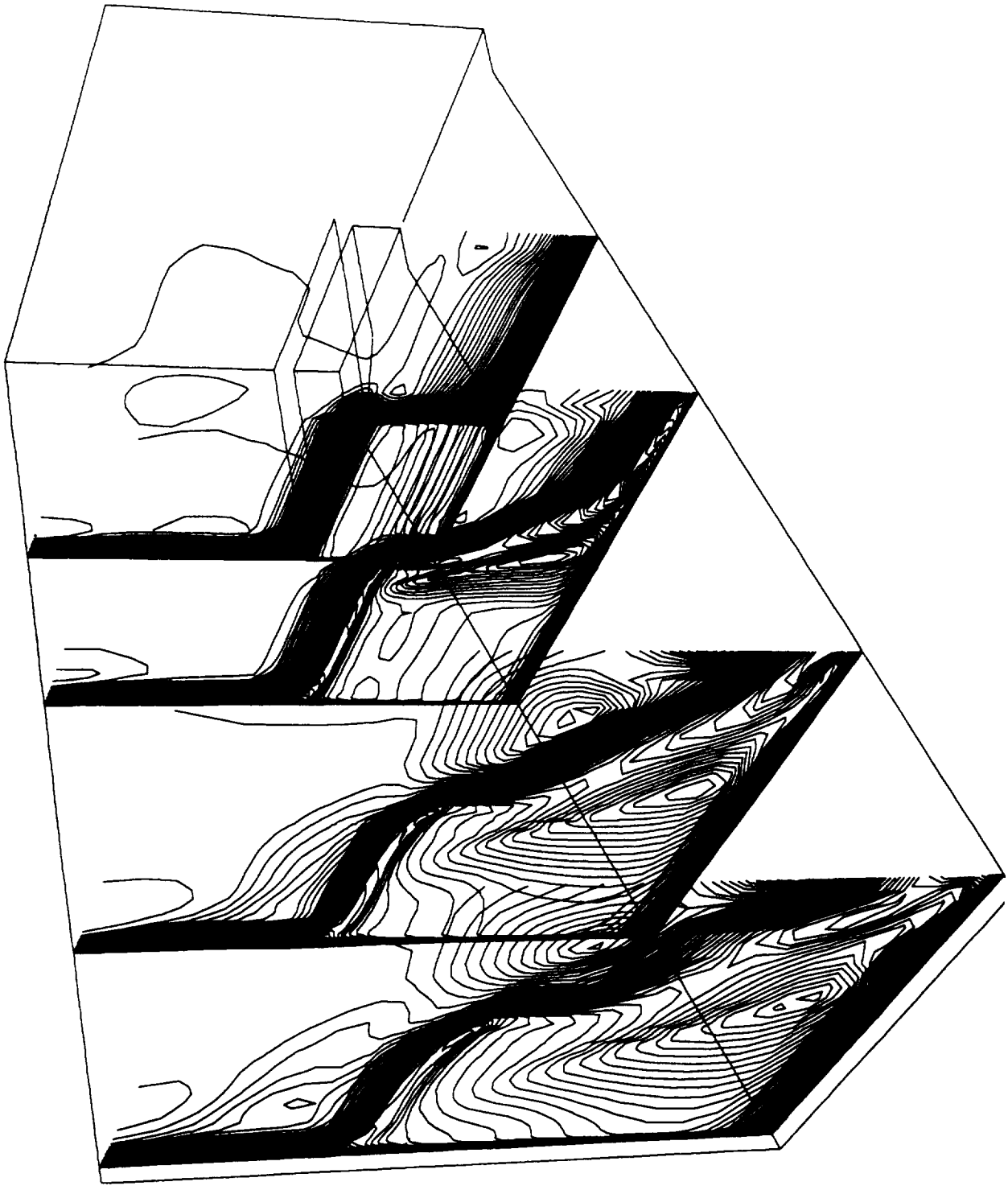

Figure 9 Mach contours depicting various crossflow (ξ-constant) planes of the nozzle-afterbody (Case 1).

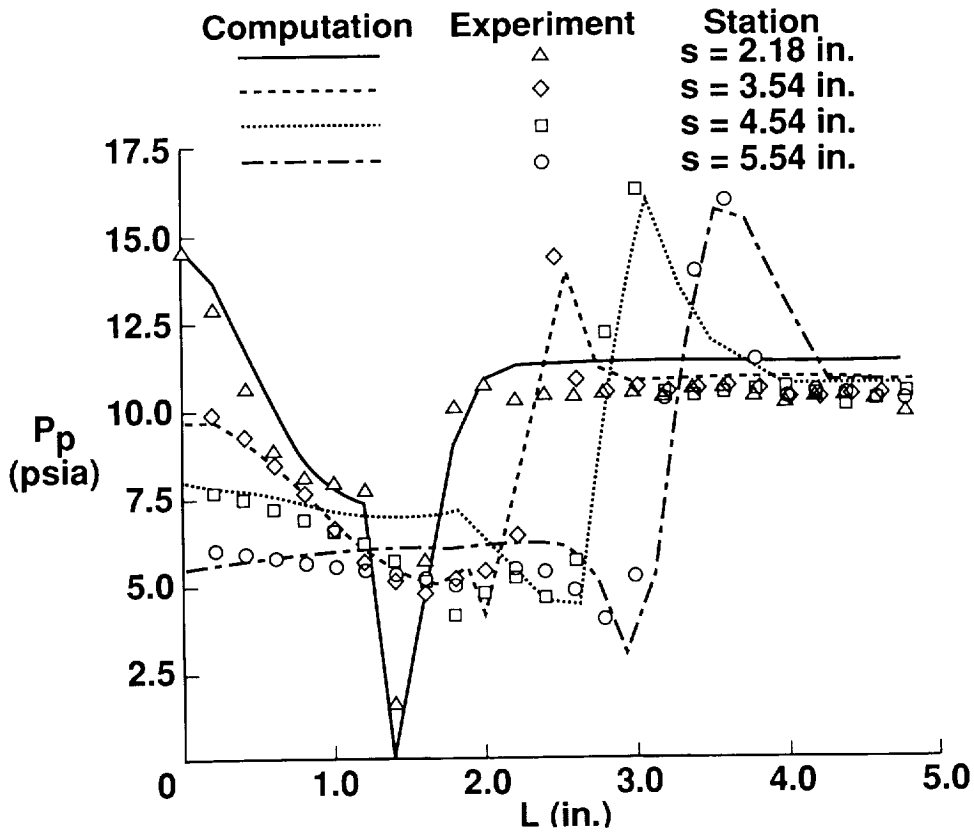

Figure 10 Comparisons of computational and experimental [3] off-surface pitot pressure (Case 1).

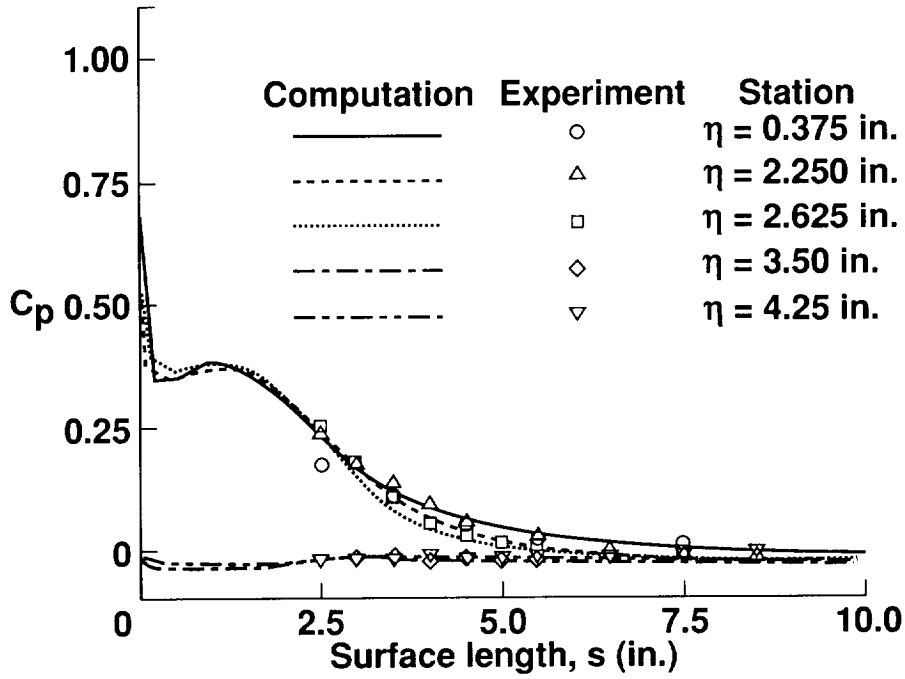

Figure 11 Comparisons of computational and experimental [2] surface pressure coefficients (Case 1).

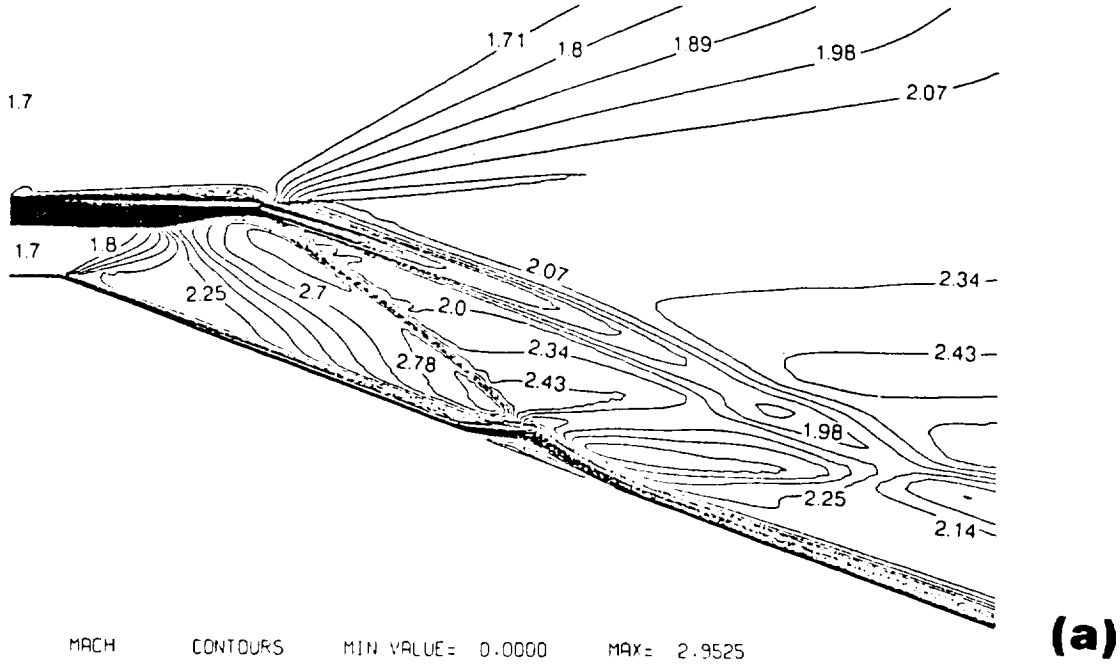

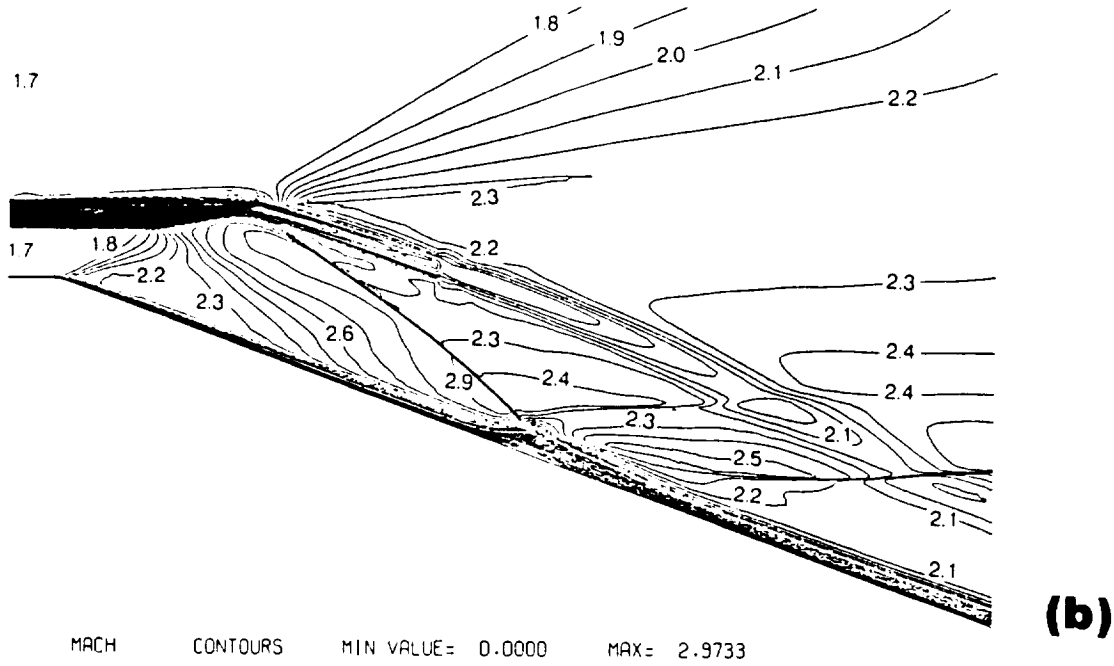

Figure 12 Mach number contours of Case 5 where the flow is overexpanded: (a) solution on the fixed grid shown in Fig. 6a, (b) solution on the adapted grid shown in Fig. 6b.

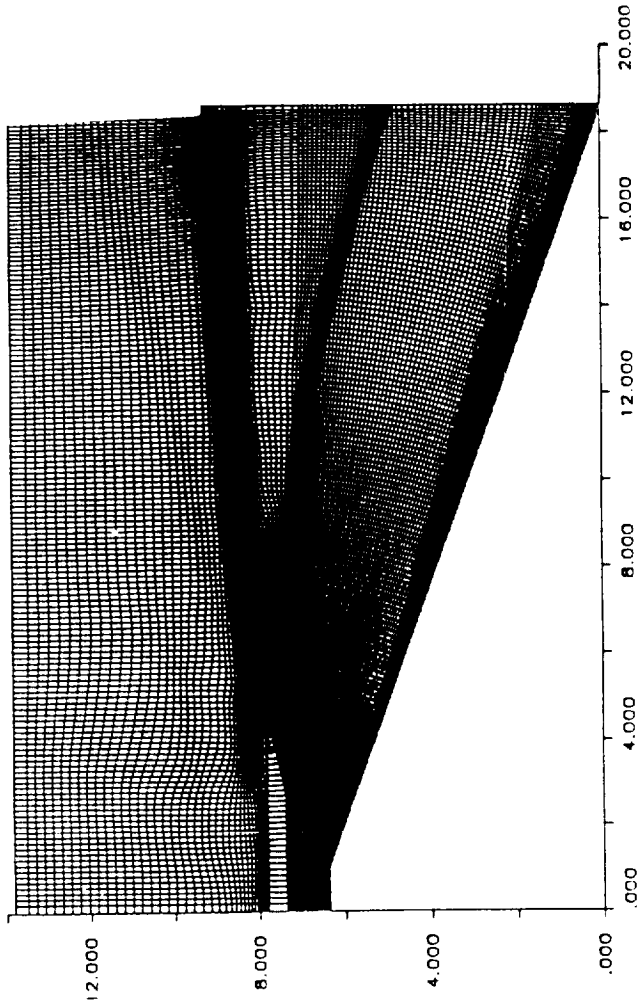

Figure 13 A flow adapted grid for a flow which is underexpanded (Cases 1–4).

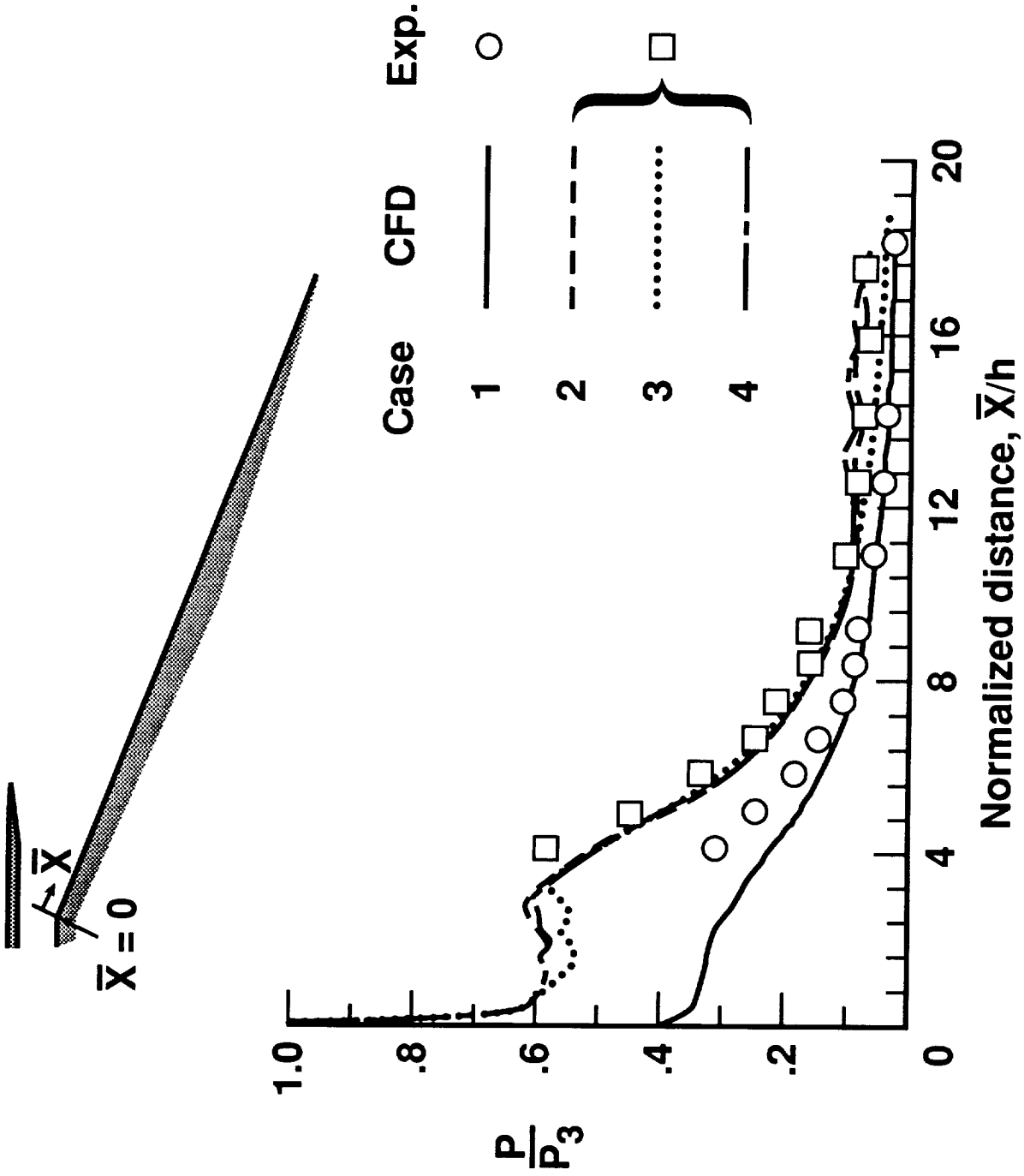

Figure 14 Comparisons of computed (2-D) and experimental [2] surface pressures.

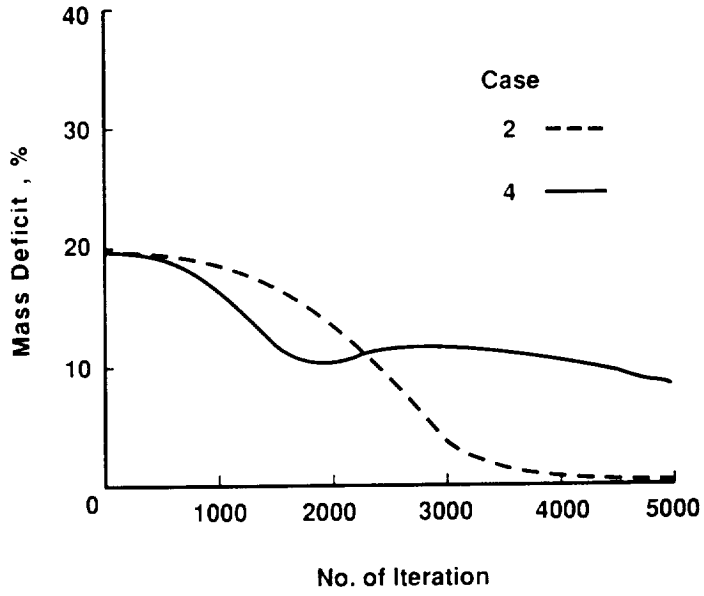

Figure 15 Global mass conservation error for Cases 2 and 4.

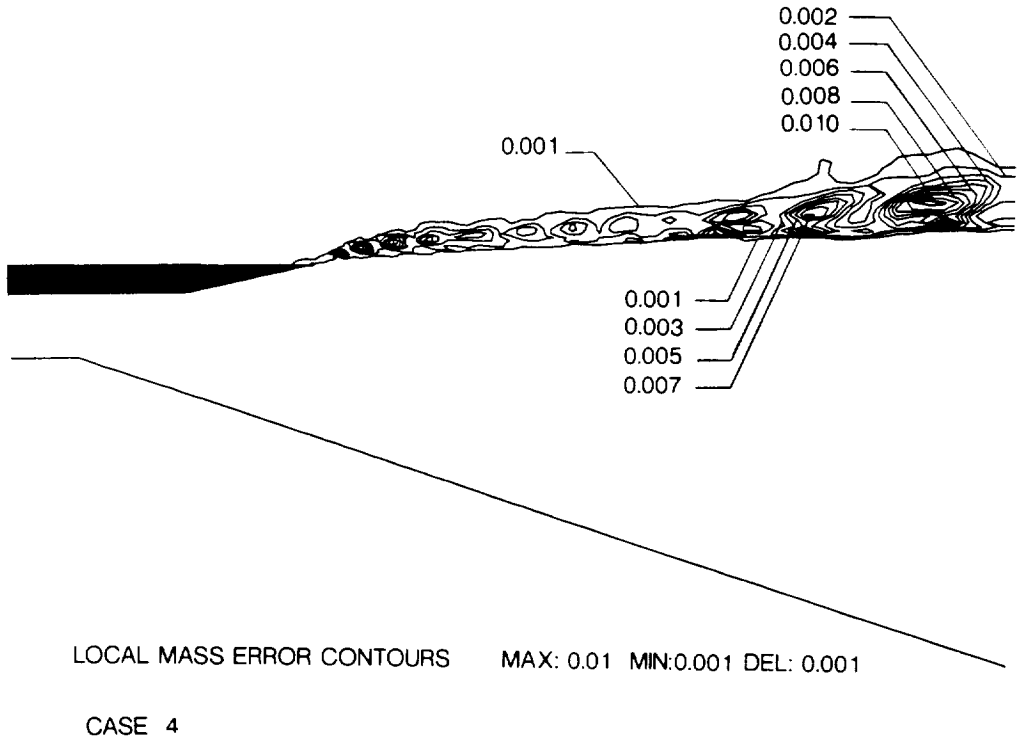

Figure 16 Local mass error due to mixing of species (Case 4).

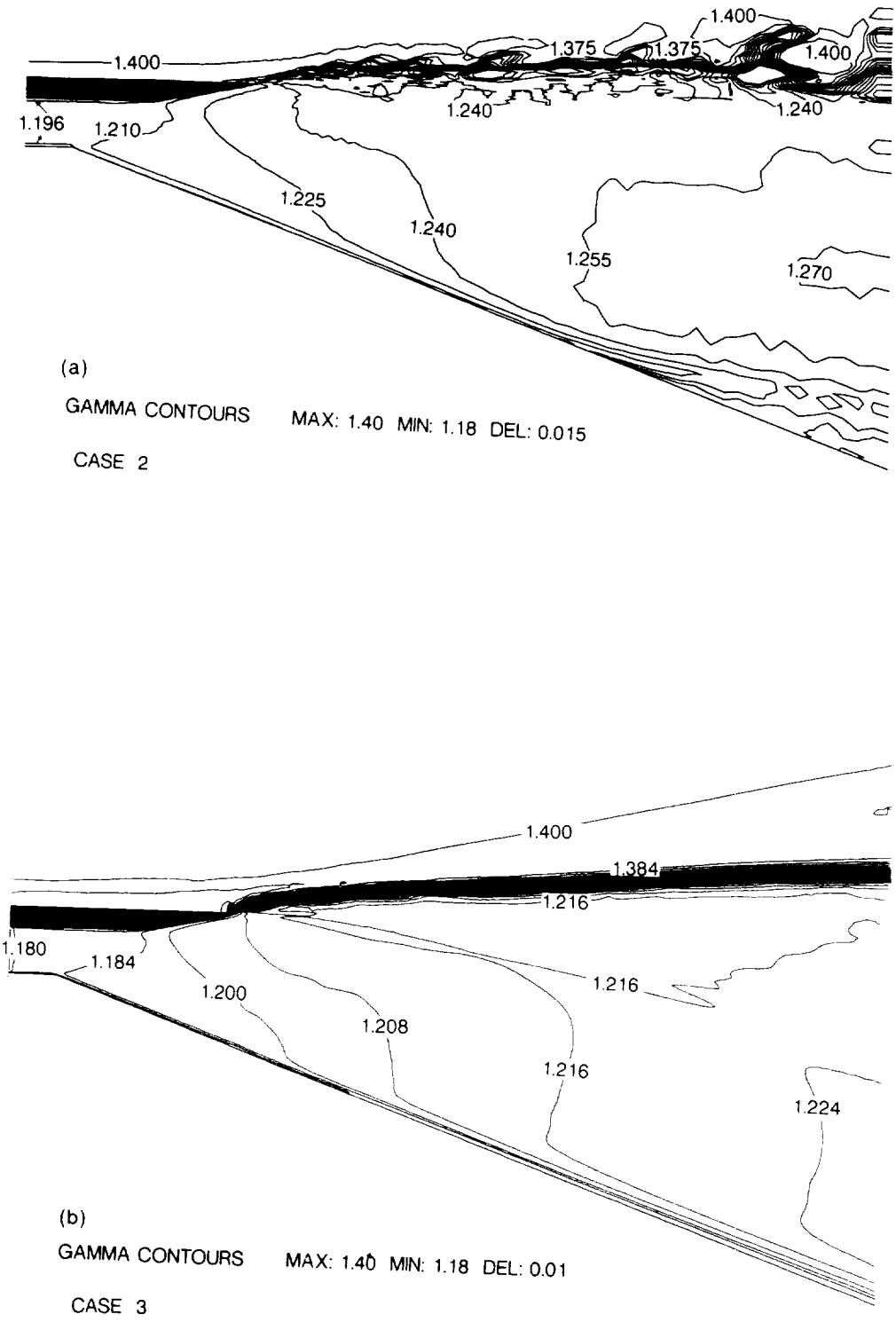

Figure 17 Contours of specific heat ratio: (a) Case 2, (b) Case 3.

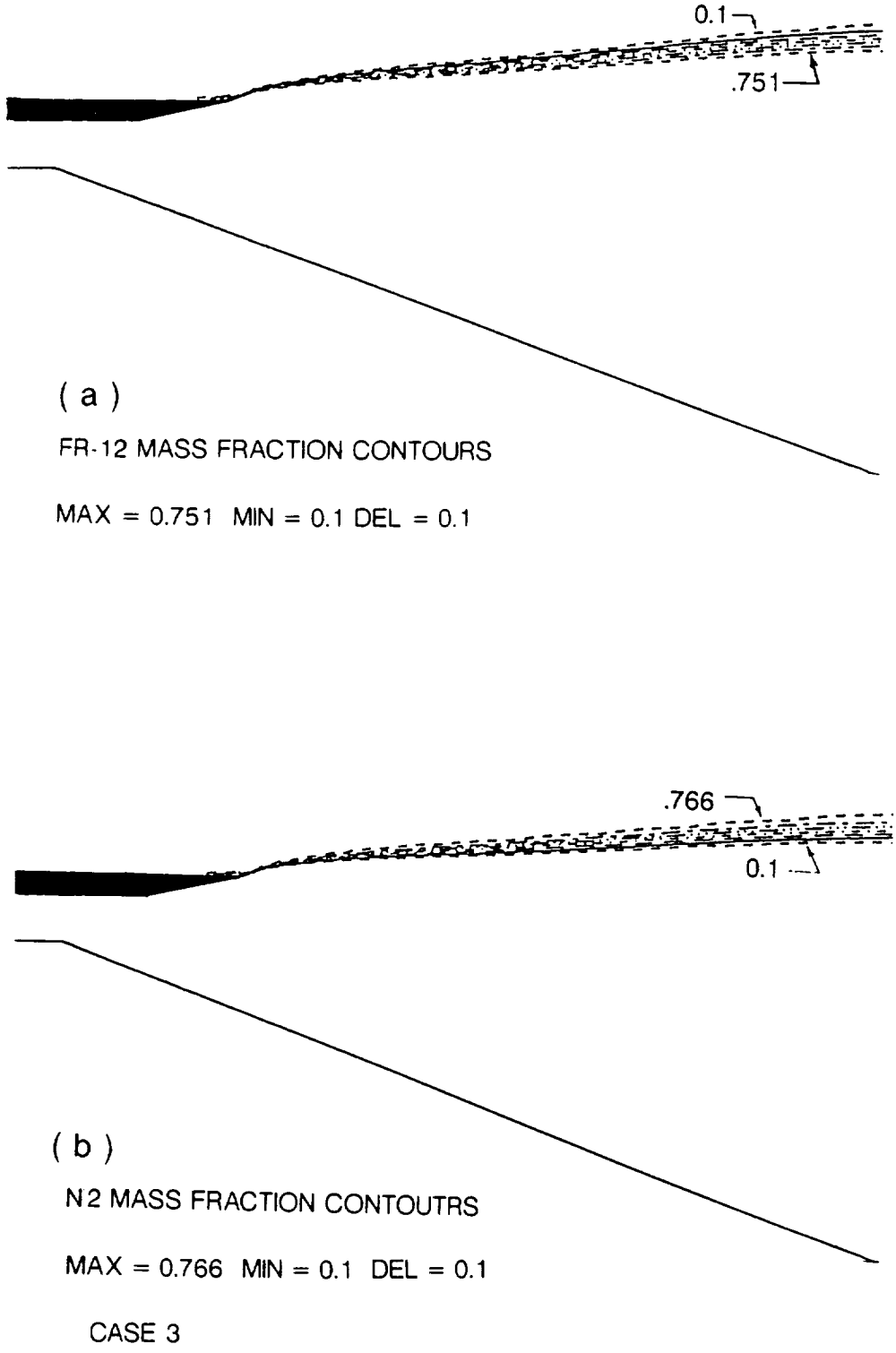

Figure 18 Mass fraction contours of Case 3: (a) Freon-12, (b) Nitrogen.

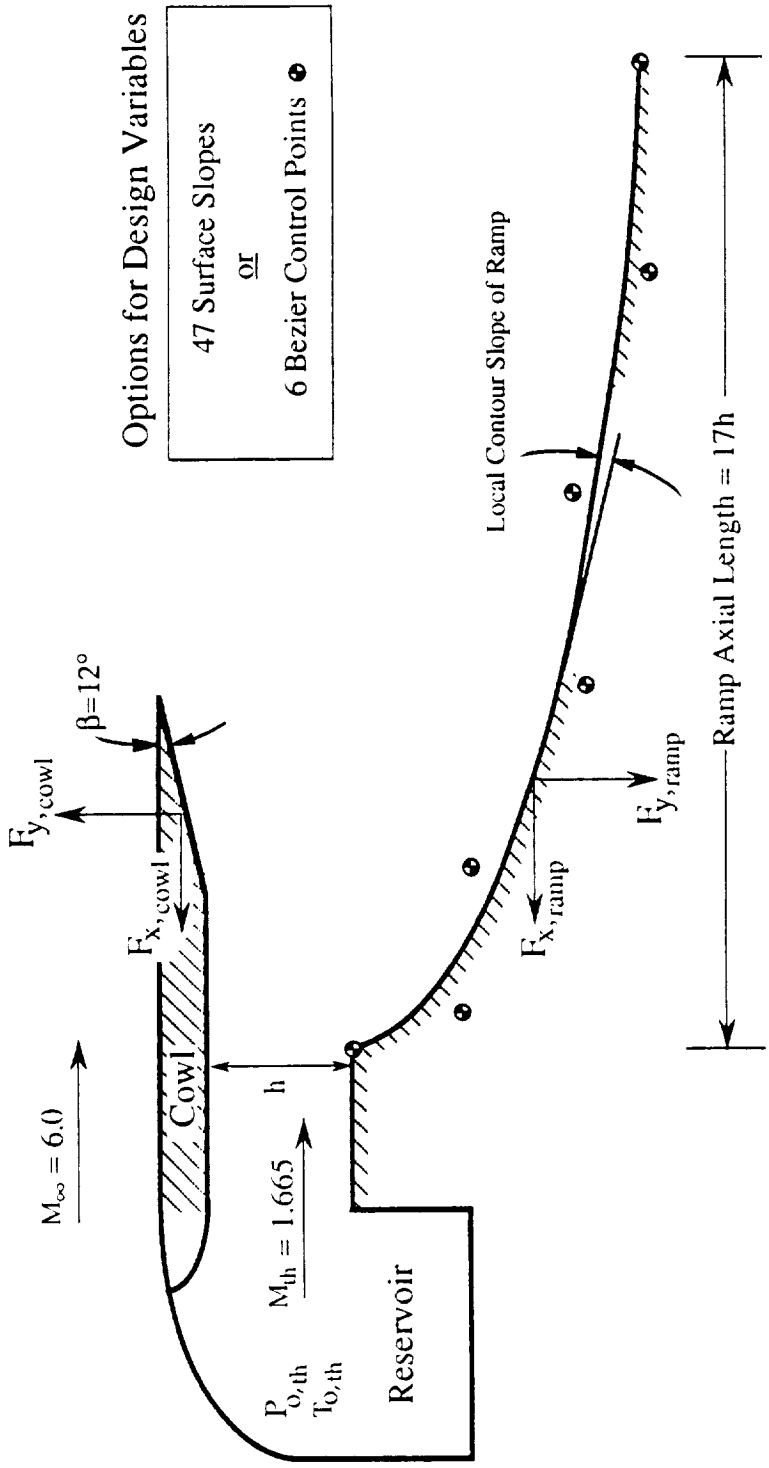

Figure 19 Physical and geometrical formulation of the nozzle-afterbody optimization problem.

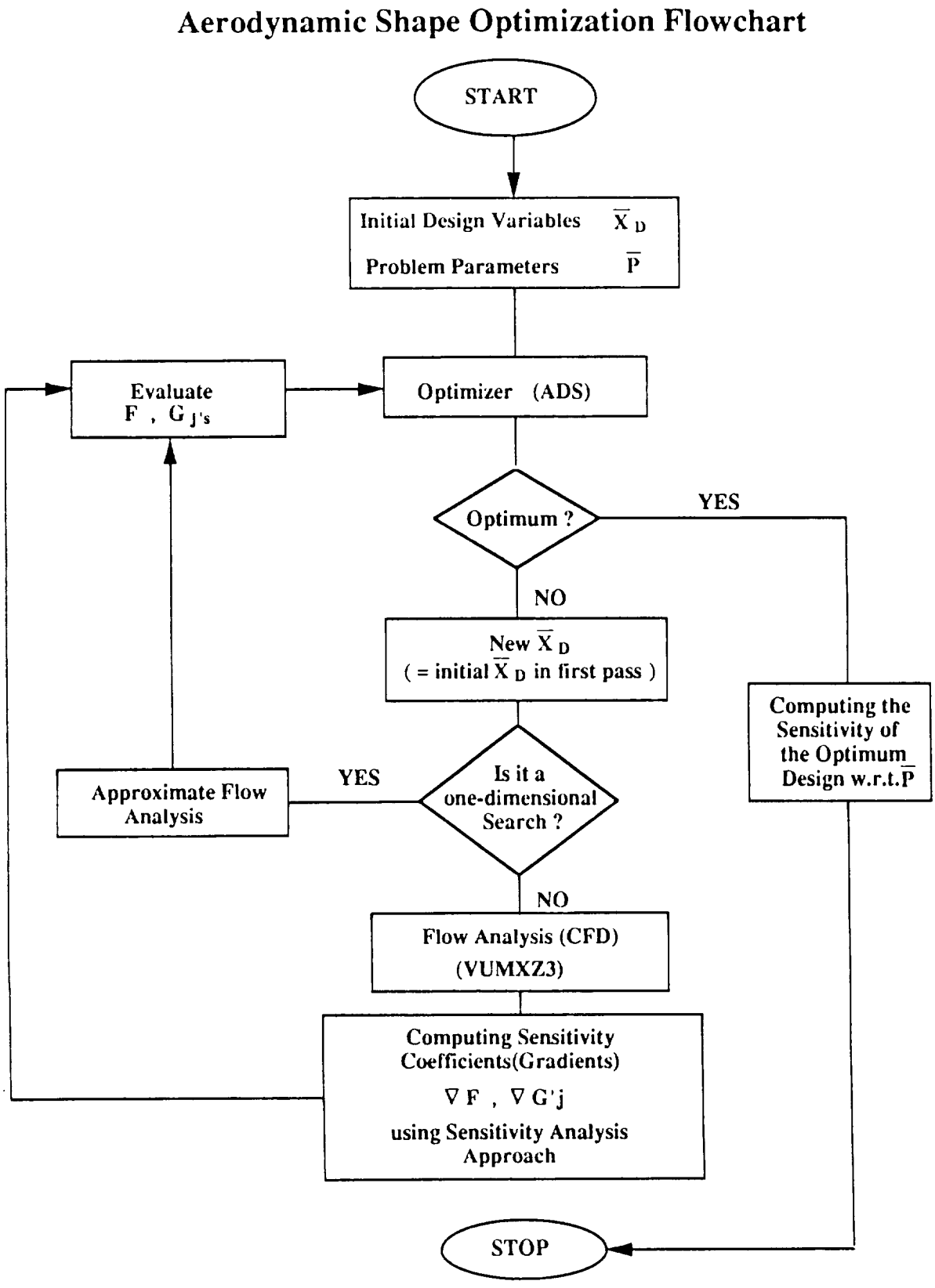

Figure 20 Flowchart of the aerodynamic shape optimization method.

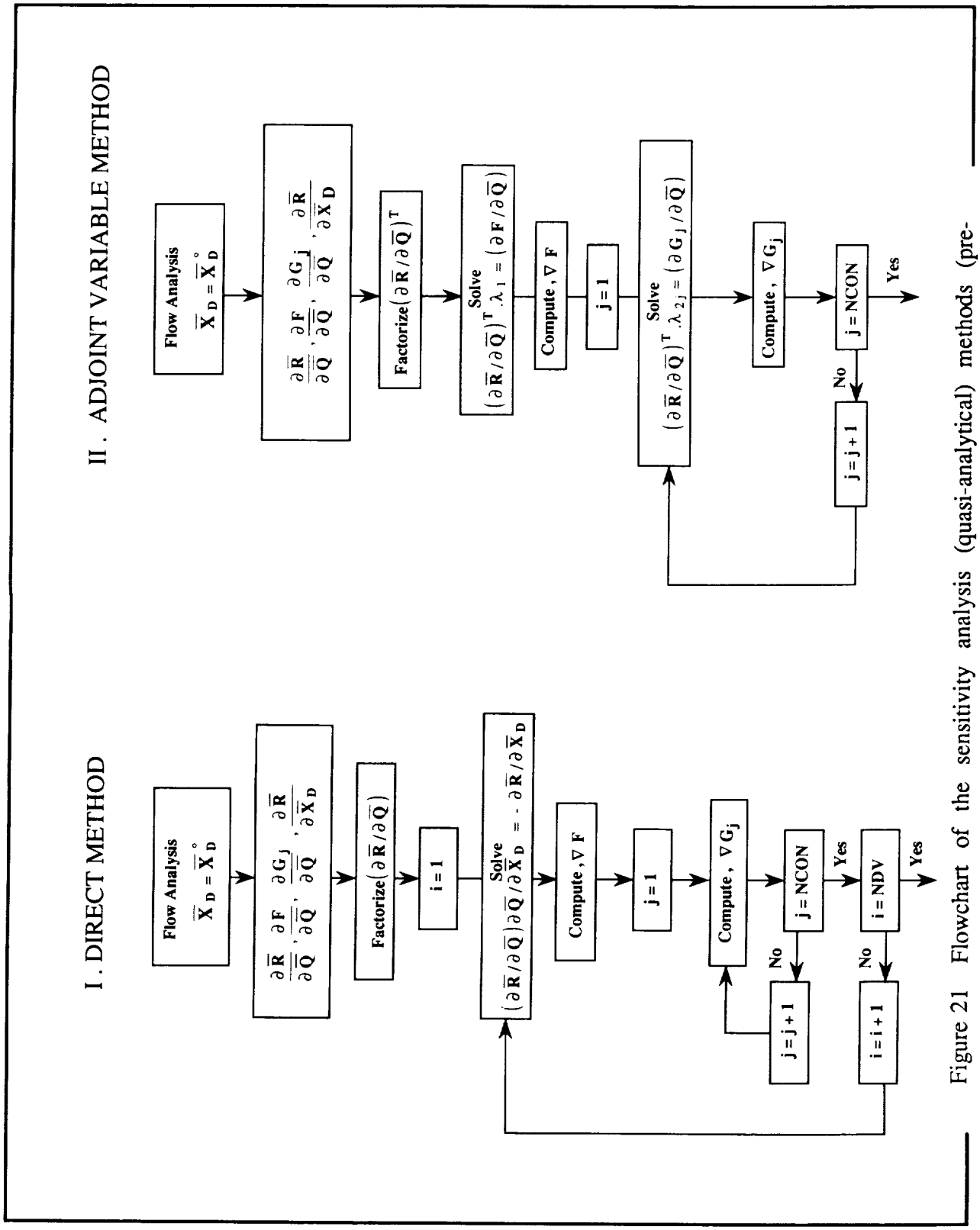

Figure 21 Flowchart of the sensitivity analysis (quasi-analytical) methods (pre-optimization sensitivities).

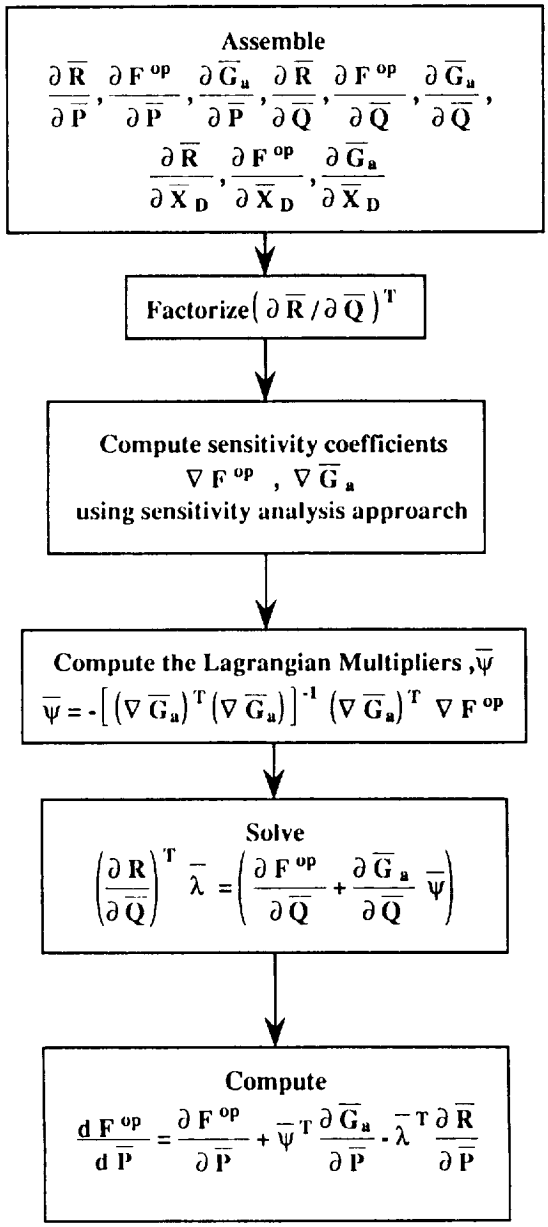

Figure 22 Flowchart of the adjoint variable method to determine the sensitivity derivatives (post-optimization sensitivities).

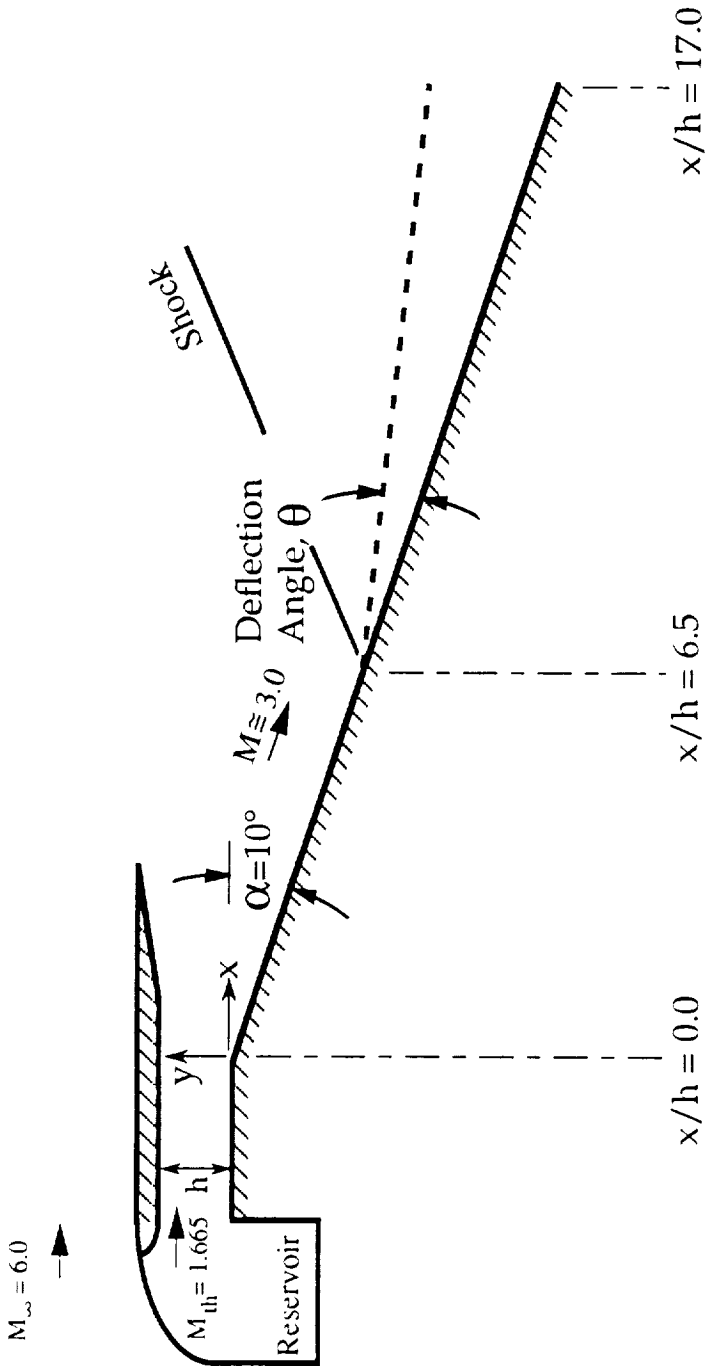

Figure 23 Description of the flowfield prediction problems.

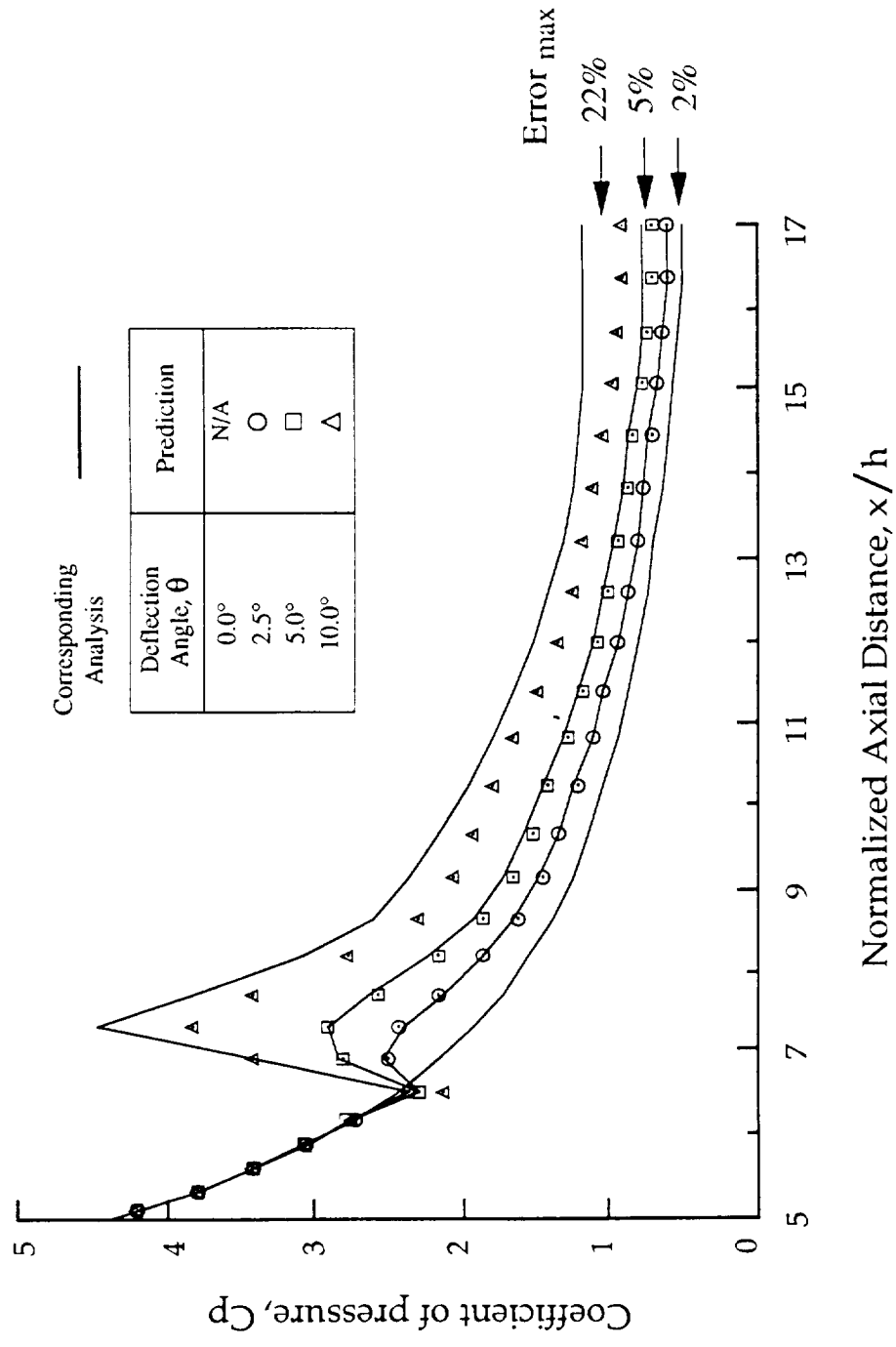

Figure 24 Surface pressure coefficient distributions along the ramp for various deflection angles (Case 6-8).

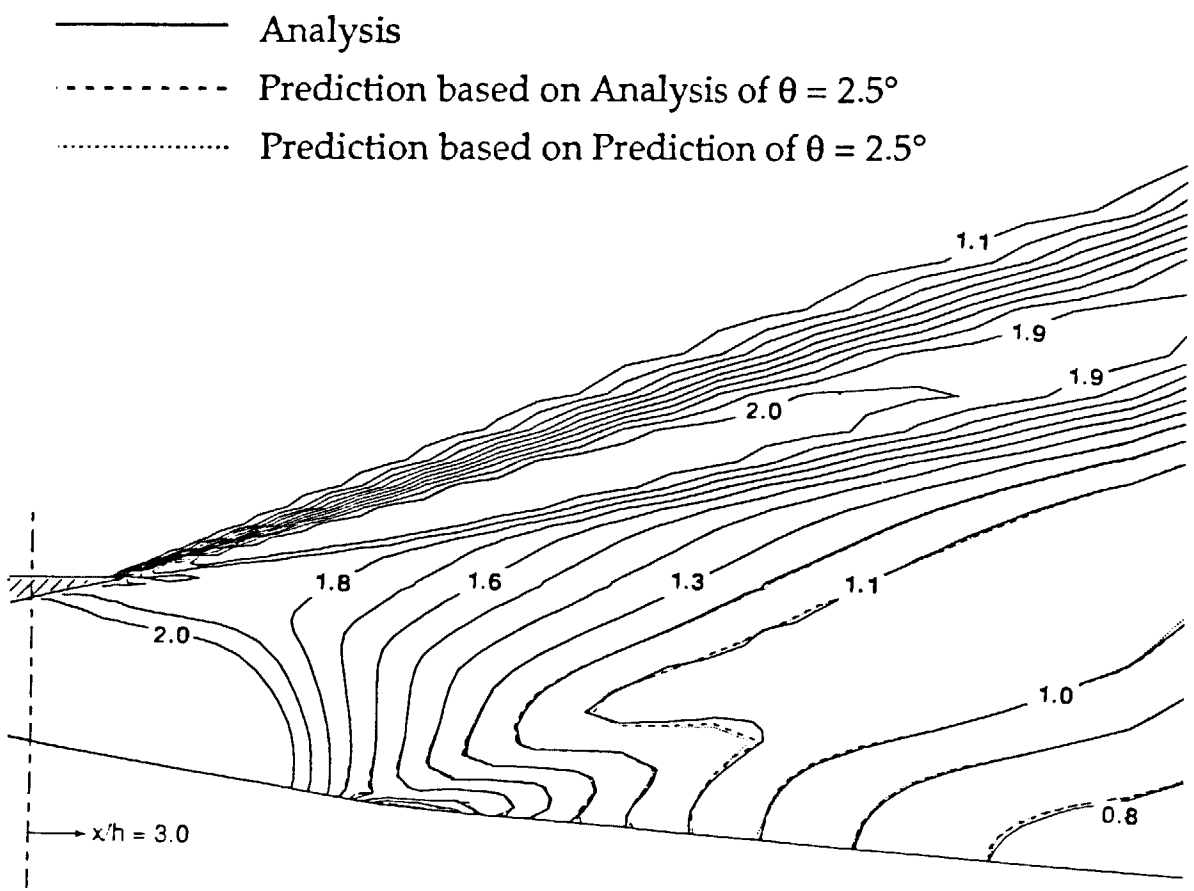

Figure 25 Comparisons of density contours for θ = 5° ramp deflection (Cases 7, 9 and 10).

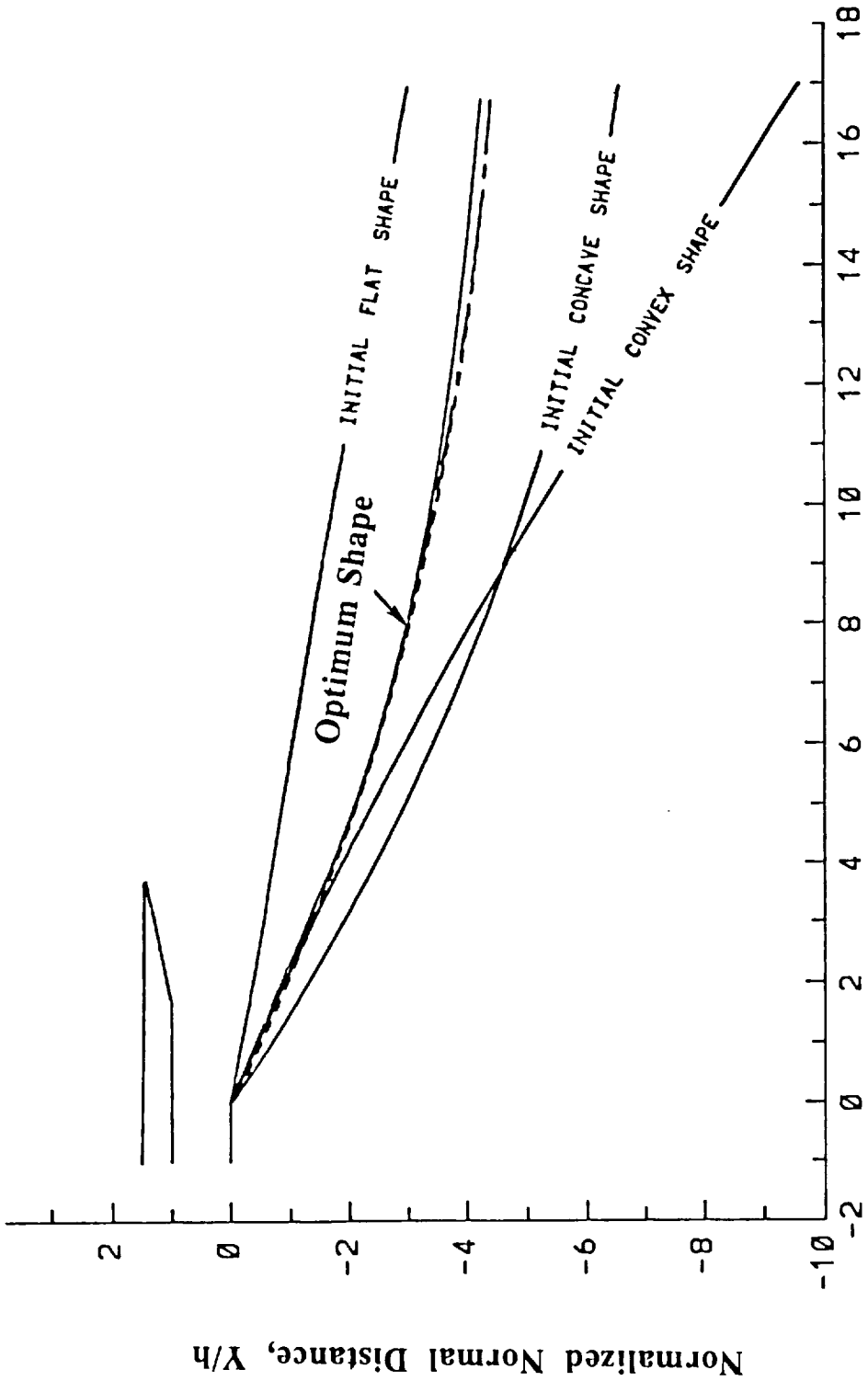

Figure 26 Comparisons of final optimized ramp shapes (Case 6, 11, and 12).

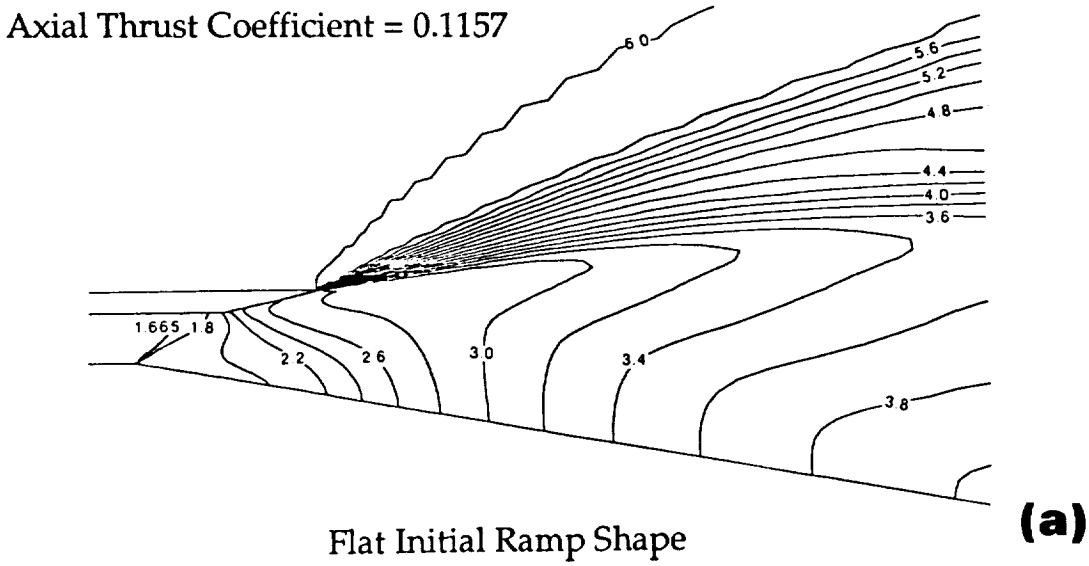

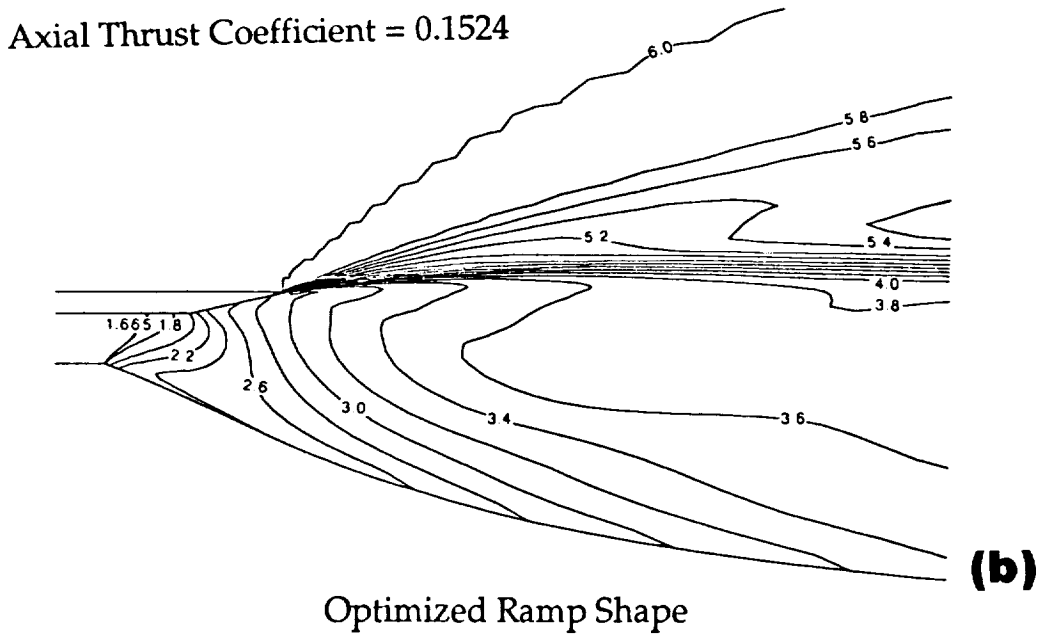

Figure 27 (a) Mach contours of the initial ramp shape (Case 6).
(b) Mach contours of the optimized ramp shape (Case 6).

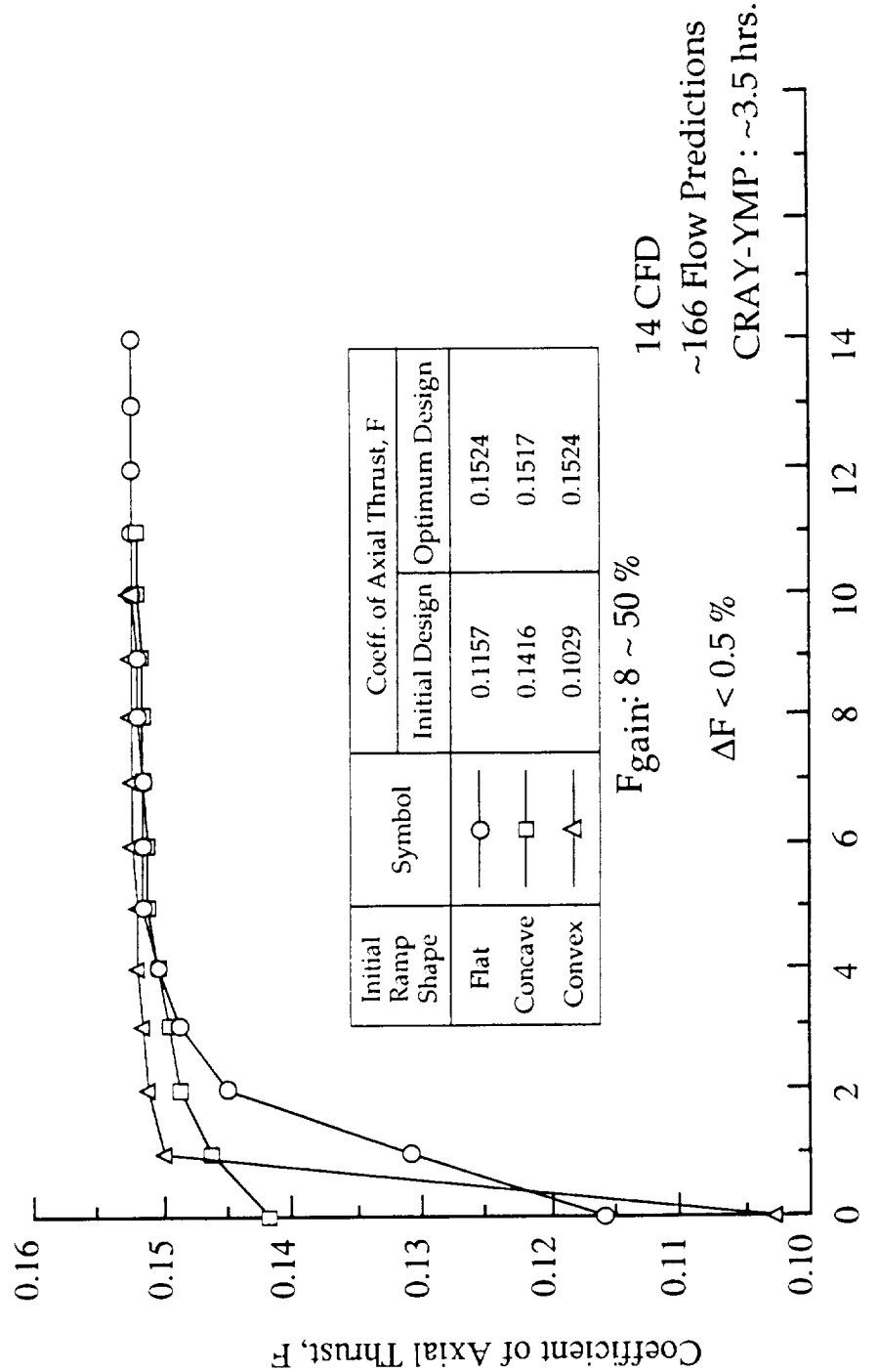

Figure 28 Optimization history of the objective function for Cases 6, 11, and 12.

REPORT DOCUMENTATION PAGE

Form Approved
OMB No. 0704-0188

1. AGENCY USE ONLY (Leave blank)	2. REPORT DATE	3. REPORT TYPE AND DATES COVERED
	April 1992	Contractor Report

4. TITLE AND SUBTITLE
Flow Analysis and Design Optimization Methods for Nozzle Afterbody of a Hypersonic Vehicle

5. FUNDING NUMBERS
G NAG1-811
G NAG1-1188
WU 505-59-30-01

6. AUTHOR(S)
Oktay Baysal

7. PERFORMING ORGANIZATION NAME(S) AND ADDRESS(ES)
Old Dominion University
Mechanical Engineering & Mechanics Department
Norfolk, Virginia 23529

8. PERFORMING ORGANIZATION REPORT NUMBER

9. SPONSORING / MONITORING AGENCY NAME(S) AND ADDRESS(ES)
National Aeronautics and Space Administration
Langley Research Center
Hampton, Virginia 23665-5225

10. SPONSORING / MONITORING AGENCY REPORT NUMBER
NASA CR-4431

11. SUPPLEMENTARY NOTES
NASA Langley Technical Monitor: David S. Miller

12a. DISTRIBUTION / AVAILABILITY STATEMENT
Unclassified-Unlimited

Subject Category 02

12b. DISTRIBUTION CODE

13. ABSTRACT *(Maximum 200 words)*

This report summarizes the methods developed for the aerodynamic analysis and the shape optimization of the nozzle-afterbody section of a hypersonic vehicle. Initially, exhaust gases were assumed to be air. Internal-external flows around a single scramjet module were analyzed by solving the 3-D Navier-Stokes equations. Then, exhaust gases were simulated by a cold mixture of Freon and Argon. Two different models were used to compute these multispecies flows as they mixed with the hypersonic air flow. Surface and off-surface flow properties were successfully compared with the experiemntal data. In the second phase of this project, the Aerodynamic Design Optimization with Sensitivity analysis (ADOS) was developed. Pre- and post optimization sensitivity coefficients were derived and used in this quasi-analytical method. These coefficients were also used to predict inexpensively the flow field around a changed shape when the flow field of an unchanged shape was given. Starting with totally arbitrary initial afterbody shapes, independent computations were converged to the same optimum shape, which rendered the maximum axial thrust.

14. SUBJECT TERMS
hypersonic nozzle-afterbody flows
mixing of multispecies flows
sensitivity coefficients
flow predictions
aerodynamic design optimization

15. NUMBER OF PAGES
60

16. PRICE CODE
A04

17. SECURITY CLASSIFICATION OF REPORT	18. SECURITY CLASSIFICATION OF THIS PAGE	19. SECURITY CLASSIFICATION OF ABSTRACT	20. LIMITATION OF ABSTRACT
Unclassified	Unclassified	Unclassified	

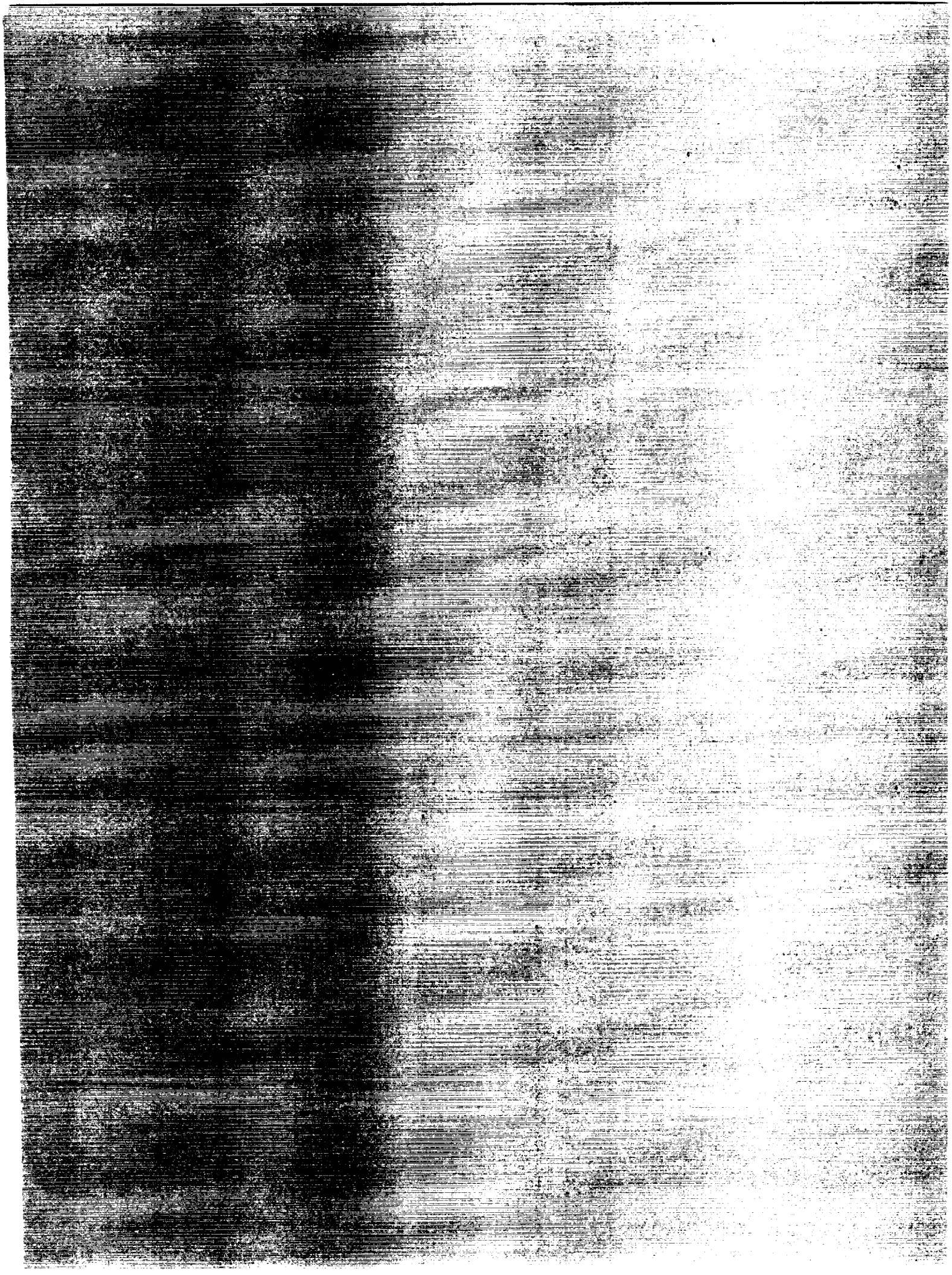

National Aeronautics and
Space Administration
Code JTT
Washington, D.C.
20546-0001

Official Business
Penalty for Private Use, $300

BULK RATE
POSTAGE & FEES PAID
NASA
Permit No. G-27

NASA

POSTMASTER: If Undeliverable (Section 158 Postal Manual) Do Not Return